

OPTIMIZATION TECHNIQUES FOR ELECTROMAGNETIC DEFORMABLE MIRRORS

by

Alejandro R. Rozene

in partial fulfillment of the requirements for the degree of Solid and Fluid Mechanics

Master of Science
in Mechanical Engineering

at the Delft University of Technology,
to be defended publicly on Tuesday April 26, 2018 at 13:45 PM.

Supervisor:	Prof. ir. J. W. Spronck	
Thesis committee:	Prof. dr. ir. H. Goosen,	TU Delft
	Dr. A. Hunt,	TU Delft
	Dr. ir. R. Saathof,	TNO

This thesis is confidential and cannot be made public until April 26, 2023.

An electronic version of this thesis is available at <http://repository.tudelft.nl/>.

ACKNOWLEDGMENTS

To the Rozene and the Vallespín families (we are too big a tribe to mention you individually). To the people who promoted me. I wish to mention R.C. Delft and the Geerweg 115 people. Finally, to the TNO Optomechanics group: The most passionate group of scientists and engineers I have met in my life; I learned so much there.

yo amo los mundos sutiles...

A. Machado

*Alejandro R. Rozene
Delft, April 2018*

SUMMARY

Light propagates through space in waves that suffer aberrations when penetrating Earth's atmosphere. These atmospheric aberrations limit the resolution of ground-based telescopes dramatically. Adaptive Optics (AO) is a technology designed for overcoming atmospheric aberrations. It enables ground-based telescopes to reach diffraction limited images. The concept of AO is to drive a Deformable Mirror (DM) to the counter-wavefront shape of the incoming aberration. This cancels the effects of the distortion and corrects the phase error. AO has its origin in astronomy but is used in other fields such as Free Space Optics (FSO), lithography or ophthalmology. TNO has developed a Deformable Mirror aimed for several AO applications. The continuous mirror surface is deformed by 57 electromagnetic actuators. These are placed perpendicular to the mirror surface and arranged in a square layout. The electromagnetic actuators are highly precise. The DM shows almost total linear behavior ($< 1\%$ deviation in displacement) and very low hysteresis ($< 1\%$), low power consumption and high actuation stroke ($> 15\mu\text{m}$). These features allow the DM to operate in open-loop thus increasing the working speed of the AO system. The TNO DM's large surface (diameter is 160 mm) makes it suitable for high power laser applications. Some design variables of the DM which could potentially lead to an increase in its optical resolution remain unstudied. This report aims to quantify the effects on optical resolution of varying design parameters of the TNO DM. Variables to be studied are: actuator layout (actuator position, number of actuators and optical aperture) and the mechanical properties of the mirror facesheet and actuators. Another aim of this report is to explain the reasons for closed-loop convergence when actively flattening the mirror resting surface. The level of flatness (measured using surface error) increases if a feedback loop is used. In practice, 6 iterations in the control loop are needed to converge to a minimum value of surface error. To meet these objectives a modeling approach was used. Two FEM models were thoroughly validated with experimental data. They were then used to simulate mirror surface deformation. They were also used to quantify changes in resolution when varying design parameters. The figure of merit used to quantify optical resolution was a set of aberration profiles. The profiles constitute a modal basis related to atmospheric turbulence: Fourier polynomials. It was found that these modes show a lower residual error than Zernike modes when reconstructing atmospheric turbulence images. The analysis of the modeled mirror resting shape showed decreasing error in flatness when a control feedback loop was used. This behavior, observed also in the prototype, had however an order of magnitude difference with the experimental results. 3 iterations were needed to reach minimum flatness convergence with the model. As opposed to the real system which needed 6 control loop iterations to achieve the best flat. Comparing different actuator distributions showed that the current layout performs better than other layouts found in literature (radial and hexagonal). It was also found that the optical aperture influences the resolution of the generated shapes. For all layouts, the error decreases with increasing fill factor. Reaching a minimum at optical aperture 90% of the total radius. The effects of varying the number of actuators were also quantified. The mechanical properties that were studied were: The stiffness of the actuator supports and the thickness of the mirror facesheet. A parameter study showed which combination of these two values gives place to the lowest surface error when generating 37 Fourier polynomials. The parameter study also allowed to extract analytical equations relating mirror thickness and actuator stiffness for the following variables: Variation of maximum deflection of the facesheet, cross coupling and width of the influence function. The results helped answer the research questions derived from the thesis objectives. For the resting shape model, an increase in the level of flatness was seen when applying a control feedback loop. This suggested that it is the geometrical configuration of the facesheet what limits the open-loop convergence to the best flat. The order of magnitude difference seen between the model and the experimental results has its origin in the noise present in the measurement data. The modeling results also showed that the layout of actuators has limited influence in optical resolution. There is, however a high influence of optical aperture on the error. Higher optical apertures give place to lower error values. The reason is that the modes of the figure of merit, Fourier polynomials, satisfy the plate-bending governing equation (as opposed to other modal basis such as Zernike modes). So, for optical aperture values with more actuators in the field of view, higher spatial frequencies and resolution are achieved. The surface error increases for decreasing number of actuators as expected. Although, error increase is higher for higher frequency modes. For lower order modes, the increase in error is not significant.

Lower order Fourier modes have also a higher weight on atmospheric turbulence correction. The parameter study of the stiffness and thickness showed that there is a combination of mechanical parameters for which the resolution of the aberration profiles is optimal. Finally, the set of analytical expressions derived from parametric modeling, allows to design DMs in terms of desired amounts of cross-coupling, power dissipation and Influence function width. This feature is interesting for scaling of the DM design and knowledge of design sensitivities.

CONTENTS

1	Introduction	1
2	State of the Art Deformable Mirrors	3
2.1	Quick Overview of Current actuation technologies	3
2.2	Requirements of deformable mirrors	4
2.3	Optimization of Deformable Mirrors	4
3	Deformable Mirror at TNO	6
3.1	Mirror Performance.	6
3.2	Active Deformation Algorithm	7
3.3	Advantages and Challenges of the Deformable Mirror	9
3.4	Research questions	10
4	Finite Element Model of a Deformable Mirror	11
4.1	Shell element parametric model	11
4.1.1	Validation of the model with Experimental Data	12
4.2	3D model of Facesheet surface	13
5	Deformable mirror layout	17
5.1	Optical Objective function	17
5.2	Layout study and fill factor	18
5.3	Variation of number of Actuators	20
6	Design Variables	22
6.1	Analytical Curves	22
6.1.1	Amplitude	22
6.1.2	Cross Coupling.	24
6.2	Width of the Influence Function	25
6.3	Parameter Study	26
6.3.1	Parameter study for 49 Actuators layout	27
7	Conclusions	29
7.1	Conclusions from the 2D model	29
7.2	Conclusions from the 3D model	29
7.3	Conclusions from the mirror layout.	29
7.4	Mechanical properties of the mirror facesheet and actuators	30
7.5	Recommendations and future work.	30
	Bibliography	31
A	2D Fourier Fourier modal basis	33
A.1	Fourier polynomials	33
A.2	Performance comparison of the Fourier set and the Zernike set.	35
A.3	Differentiation of the Fourier polynomial terms for the bi-harmonic equation	37
A.4	General derivation for Polar coordinates	38
B	Layouts performance	39
B.1	Power consumption.	39

B.2 Atmospheric turbulence compensation for different layouts and values of the fill factor	39
B.3 Different actuator counts in direct reconstruction of Kolmogorov Phase maps	40
C Assembly of the 3D model	41
C.1 Extrapolation of Interferometer image and preparation of data	41
C.2 SolidWorks processing	42
C.3 FEM Analysis	43
C.4 Processing in MATLAB	45
D Parametric Modeling	47
D.1 MATLAB-ANSYS coupling.	50
E Constant width of the influence function	52

1

INTRODUCTION

Modern astronomy faces challenges such as understanding the evolution of the early universe and the presence of exo-planets. For instance, detection of light coming from extra-solar planets would help gain more knowledge about their composition and temperature. Increasing the knowledge of the universe motivates the development of more powerful astronomical tools that can capture photons which are currently lost by interference with brighter stars [1].

Astronomical telescopes are evolving towards bigger primary apertures. Larger apertures allow to capture more photons, make dimmer objects visible and obtain more resolute images. However, for ground based telescopes resolution is also limited by atmospheric turbulence. Atmospheric turbulence induces variations in the refraction index of air due to fluctuations in temperature [2]. This effect modifies the optical path lengths (OPL) of light causing images to be dimmed by phase errors (or wavefront aberrations) [3].

Adaptive Optics (AO) is a technique developed for compensating wavefront aberrations. It theoretically allows ground-based telescopes to achieve diffraction-limited resolution. Adaptive Optics systems correct wavefront aberrations by deforming the surface of one or more Deformable Mirrors (DM). The shape adopted by the DM is the counter-wavefront of the incoming light. The result is a reflected image with diffraction limited resolution. Wavefront aberrations are previously measured by splitting the beam to a wavefront sensor. A control computer processes the wavefront information and sends deformation commands to the mirror's actuators [3].

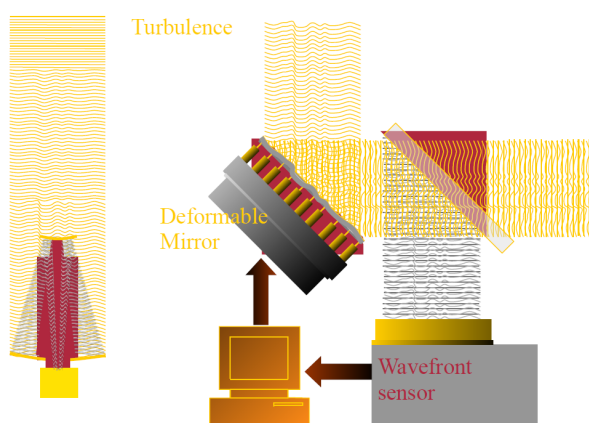


Figure 1.1: Schematic of an Adaptive Optics system. The leftmost figure is a telescope, the right figure the AO scheme. Source: *D. Mawet. Astronomical Measurements and Instrumentation*

Modern ground based AO systems combine deformable mirrors in several layouts. This increases the correction of atmospheric turbulence accounting for errors introduced by the inclination of the measured beam and other. They also use powerful laser beams (Laser Guided Stars (LGS)) to measure the aberrations caused by the atmosphere. Multi-Objective Adaptive Optics (MOAO) uses multiple laser guided stars to attempt

a high Strehl ratio for small Fields of View (FoV). The Multi-Conjugate Adaptive Optics (MCAO) layout attempts a high Strehl ratio over large FoV within larger uncorrected fields [4]. This technique combines several LGS and DMs at different angles. Extreme AO systems (xAO) are meant to make a high order correction of the aberrations so as to limit light diffracted by residual wavefront errors. They combine AO with methods such as coronagraphy to reduce scattered light and detect planets close to bright stars [5]. These AO layouts used in Extremely Large Telescopes (ELTs), require open-loop operation to improve light performance [6]. For high speed applications iterative control loops limit the temporal performance of the Adaptive Optics System. Open-loop operation on the other hand increases the speed but requires sensing the wavefront before it reaches the DM (as opposed to closed loop where the WFS is placed after the DM). These technologies present design challenges for DMs by requiring from them: higher speeds, higher resolution and bigger apertures.

Astronomy is not the only field of application for AO. It also finds applications in ophthalmology [7], Free Space Optical communication (FSO) [8] and some industry applications such as lithography [9]. For lithography, the aberrations to be corrected are introduced by the laser, which heats and deforms the mirror surface. In ophthalmology the aberrations to be corrected are those found in the human eye. Low order Zernike modes describe the aberrations concerning these applications.

FSO is a communication technology which is increasing its importance mainly driven by the saturation of the RF spectrum. In FSO, as well as in astronomical applications atmospheric turbulence-induced distortions are a major limitation to the performance of the system [8]. Another challenge to beat in FSO is time transfer which has direct relation to tip-tilt correction [10].

Adaptive Optics is a growing technology in which several challenges and limitations are still present. Many of the present challenges are related to the speed and the resolution of the measurement systems. AO also has a broad range of applications. This thesis aims to increase the performance of an existing DM manufactured by TNO. The DM is aimed to serve more than one AO application. This thesis is divided into six chapters including the current one. Chapter 5.2 discusses the state-of-the-art technologies for Deformable Mirrors. Chapter 3 briefly describes a DM developed at TNO and introduces the research questions that motivated this study. In chapter 4, a Finite Element Method (FEM) model for a Deformable Mirror surface is presented. Chapters 5 and 6 discuss the findings on the influence of modifying some design variables of the DM. Chapter 7 concludes the report giving recommendations and stating future work.

2

STATE OF THE ART DEFORMABLE MIRRORS

Chapter two presents a quick overview of state-of-the-art DMs for astronomical purposes. An overview of currently used actuation technologies is presented together with their advantages. The current requirements of DMs for common astronomical applications are discussed. Finally, the main optimization techniques found in literature to increase the performance of DMs are discussed.

2.1. QUICK OVERVIEW OF CURRENT ACTUATION TECHNOLOGIES

The technological choice of a DM is driven by the application for which it is intended. And by the environmental and mechanical conditions under which it will operate [4].

Deformable mirrors can be classified into segmented DMs, membrane DMs, liquid crystal DMs or continuous DMs in terms of their facesheet [3]. In this section only continuous mirror actuation technologies are discussed. In continuous-type mirrors, a continuous reflective surface is actively deformed by a set of actuators connected to it. There are currently four actuation technologies available in the market.

Stacked array DMs are deformed by ferroelectric actuators made of stacks of individual segments (either piezoelectric or electrostrictive). An electric field applied through the stacks changes their dimensions resulting in actuation in the plane normal to the mirror surface. Bimorph DMs are similar to stacked array DMs. They work based on the transverse piezoelectric effect. Application of a voltage through an electrode parallel to the mirror gives place to local elongation which induces curvature in the mirror surface. MEMS (Micro Electro Mechanical System) DMs use MEMS device as actuators based on different MEMS technologies. Finally, electromagnetic DMs have actuators glued to the rear face of a thin mirror [4].

The choice of actuation technology requires a thorough evaluation of the advantages and limitations of the available solutions: stacked array DMs have higher power consumption and limited stroke. Their intrinsic hysteresis cycles require large amounts of electronics to correct it. But they come at a low cost, due to ease of production. They have a high density of actuators thanks to the small plate thickness, and are extremely stiff. This allows for short response times (first eigenfrequency > 10 kHz). Bimorph DMs are even easier to manufacture than stacked array DMs. But the size of bimorph DMs is limited by the resonant frequencies of the system (in the hundreds of Hz range), limiting the number of actuators that can be used. Electromagnetic mirrors have high stroke due to the efficiency of voice coil actuators. But they are bulky, giving place to large actuator pitch values. They have fast response times (up to < 1 ms). And come at a higher price. Electromagnetic actuators typically require high actuation voltages. MEMS DMs have a high density of Actuation points but a very limited stroke. Choosing the appropriate solution depends strongly on the requirements to be met by the AO application [4].

2.2. REQUIREMENTS OF DEFORMABLE MIRRORS

The requirements of an Adaptive Optics System are defined in the error budget, which must meet the desired degree of correction (at a specific operation wavelength). Current AO systems face limitations in fitting atmospheric images (fitting error), time lag, noise and spatial aliasing [11]. The first three terms are related to the DM directly.

The error of a DM is measured using the total variance of the common error sources. It can be distributed into the following components: atmospheric fitting error, measurement or noise error, time lag error and anisoplanatic error [12], [13].

Only the fitting error and the noise or noise error will be treated in this document. The fitting error has its origin in the limited Degrees of Freedom (DoF) of the DM for the correction of atmospheric turbulence. The measurement error is caused by the inherent noise present in the measurement devices.

Most science instruments will use the Strehl ratio to determine the allowed residual surface error RMS in the mirror surface (see equation 4.1.1). The Strehl ratio is defined as the ratio of the maximum intensity in a Point Spread Function (PSF) from a science instrument to a theoretically perfect point [2]. A good approximation is:

$$S_r \approx e^{-\sigma_\lambda^2} \quad (2.1)$$

Where $\sigma_\lambda = \sigma/\lambda$ and λ is the wavelength. Residual error requirements vary per scientific application. For SCAO systems the requirement is ≈ 1830 nm (for 0.7 arcsec seeing at $0.5 \mu\text{m}$). For MCAO systems the requirement is 1330 nm. In XAO systems, error should meet a residual RMS of 520 nm (for 0.6 arcsec seeing at $0.5 \mu\text{m}$) [4]. This error includes the contributions of all the described terms. The fitting error corresponding to the DM should be (according to [4]): 330 nm for SCAO and MCAO, and 32 nm for XAO.

Requirements for the stroke of the actuators depend on turbulence and operation wavelength, as well as telescope diameter. For 8 m telescopes, values are in the order of $10 \mu\text{m}$. 40 m class telescopes require strokes of up to $70 \mu\text{m}$ [4]. These high stroke requirements are usually met using a woofer-tweeter arrangement [14]. In this arrangement two DMs correct atmospheric aberrations. A high stroke mirror accounts for low order aberrations. A high actuator count mirror compensates higher order (and lower amplitude) errors.

The diameter of a DM does not pose a challenge for smaller (8 m class telescopes). But bigger instruments, 30 m class telescopes, require 30 cm diameter DMs [15].

Besides the mentioned requirements, DMs need to be reliable (less than 5% failed actuators over 5 year periods). It is also important for DMs to have low power dissipation rates and work with low voltages as indicated by [4] and [15].

2.3. OPTIMIZATION OF DEFORMABLE MIRRORS

In order to increase the quality of the design of different types of DMs, several authors have proposed techniques for their optimization. Two approaches were identified: a first group of authors evaluates the geometrical layout of discrete or continuous actuators seeking for an optimal arrangement of actuators. A second group of authors modifies the mechanical properties of the DM with the objective of increasing optical performance.

Authors who modify the layout of actuators, make use of numerical methods and models. The numerical approach allows to test different layouts and determine which layout reproduces figures of merit with more fidelity¹. [16] uses FEM models to describe unimorph and bimorph mirrors. Then, by testing different actuator electrode patterns (radial and hexagonal in different combinations), determines which patterns give higher fidelities and stroke. Up to 14 Zernike modes serve as an objective function. It is concluded that for unimorph and bimorph mirrors, wide radial actuator patterns are most precise solution. An outer ring of actuators is shown to increase amplitude. [17] uses numerical models to compare turbulence correction performance of different mirror types. The considered mirrors are piston, thin plate and membrane mirrors. Actuator structures are: hexagonal, segmented ring and orthogonal. This paper concludes that actuator geometry does not play a significant role when correcting Karhunen-Loève modes, as long as actuators are distributed homogeneously. [18] optimizes surface parallel actuators using shape-optimized patterns with several planes of symmetry. It is also shown that reducing the pupil size diameter improves the correction of the first 25 Zernike modes. [19] proves that in order to generate Zernike modes in a circular facesheet, actuators need to be placed outside of the pupil aperture. The shape of Zernike modes cannot satisfy the plate

¹Fidelity is the inverse of the rms deviation of the achieved mirror shape from a target

equation using point loads only within the design domain.

Another approach found in literature is to optimize the mechanical properties of the DM. To minimize actuator induced high-frequency errors, [20] uses a parametric FEM model that modifies the length of surface parallel actuators. This consequently changes the shape of the influence function. It is demonstrated that changes in mirror substrate and actuator geometry (which could be considered as modification of stiffness properties) can reduce residual errors. This is shown by correcting for defocus. [21] in a similar approach also mentions the effect of the substrate in the shape of the influence function. [22] optimizes the facesheet and support wall thickness with shape variables. [23] makes use of a Genetic Algorithm, a heuristic optimization scheme, to solve the location problem for a finite number of candidate locations.

One common factor to all the scientific literature found is the use of Zernike modes as a figure of merit for actuator placement and mechanical parameters optimization. Zernike modes have been proven useful for modal decomposition in the past. They also conform an orthonormal basis with respect to polar coordinates. But in most astronomical applications other basis functions are used. Some authors like [13] do use Fourier (and other) modal basis for phase map reconstruction.

3

DEFORMABLE MIRROR AT TNO

Based on the philosophy of the deformable mirror from [12], a new DM concept has been developed by TNO [24]. It is a lightweight continuous mirror based on electrostrictive actuators. The purpose of the system is to remain modular. This allows to fit the DM to different applications making only small variations to the design. The DM is expected to have open-loop capabilities due to the high linearity seen in [24] where high stroke is demonstrated. The DM has 57 electrostrictive actuators glued to the facesheet and arranged in a square layout with a pitch of 18 mm occupying the circular area of diameter 160 mm of the 1 mm thick silicon facesheet.

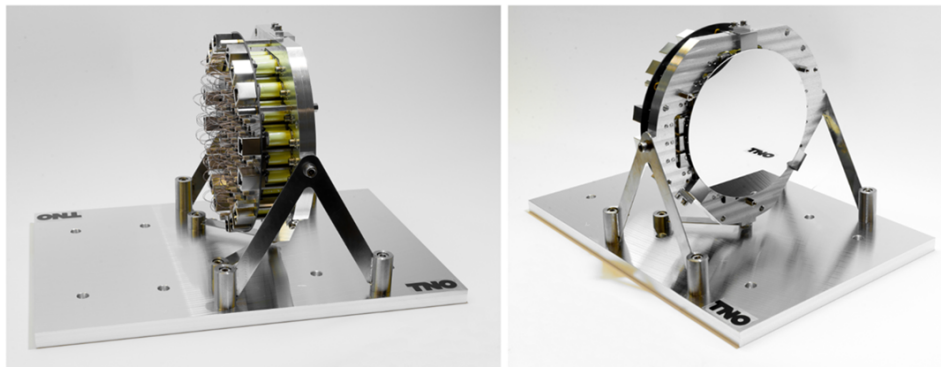


Figure 3.1: Prototype of the Electromagnetic Deformable Mirror developed by TNO. *Source: TNO*

Tests with an interferometer were carried out to measure different parameters: linearity of the response of the actuators and hysteresis of the actuation components. This measurements were done using a Fizeau interferometer and a real time computer that drove actuation commands to the DM. With the collected data it was possible to identify the performance of the DM and the actions required to increase it. giving place to the research questions of this thesis.

3.1. MIRROR PERFORMANCE

A set of step-increasing actuation currents were supplied to individual actuators of the DM. At each current step the deformation of the interface was measured with the interferometer and processed to extract the Peak to Valley value. The DM exhibited high linear behavior $< 1\%$ and hysteresis $< 1.5\%$ [25].

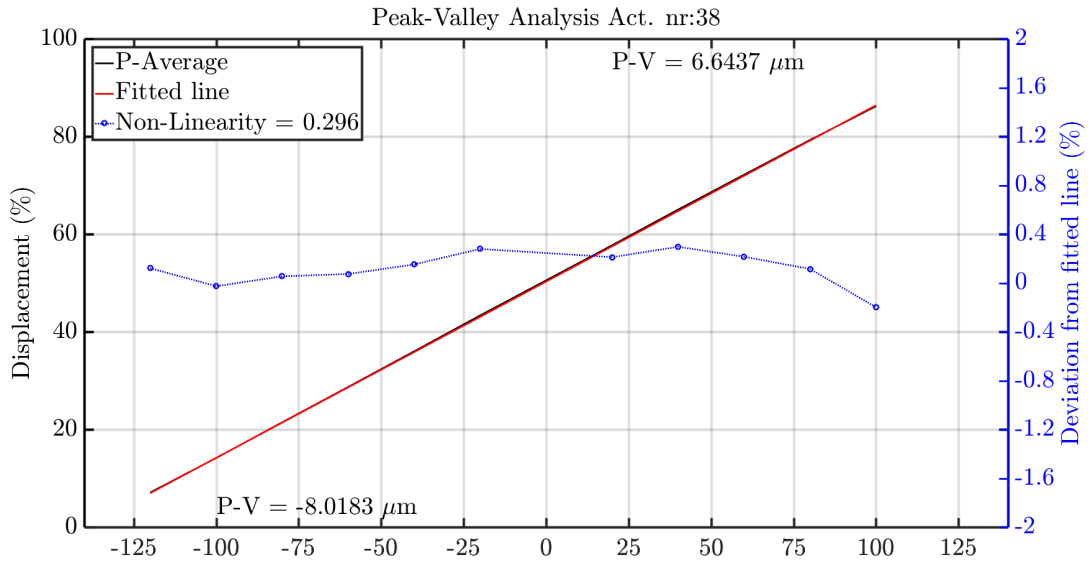


Figure 3.2: Linearity of actuator displacement. Peak to Valley test for single actuator and increasing currents. Currents range from -120mA to 120mA . Blue curve is deviation from a fitted line and shows highly linear behavior. Source [25]

This high linearity characteristics permit the use of the system in open-loop operation, where linearity assumptions are crucial.

3.2. ACTIVE DEFORMATION ALGORITHM

The displacement field resulting from the response of a single actuator is commonly called an influence Function (IF) [16]. To measure the influence functions of the mirror, interferometer images of the mirror were captured for each actuator. For this, a constant current intensity load I_n was applied to each actuator at a time. Images were recorded using a Fizeau interferometer.

The combination of all IFs forms the basis for the shape reconstruction algorithm and is shown in figure 3.4. With the obtained data, shape reconstruction can be achieved using weighted deformations of the IF's. The deformation input is obtained with a least square fit to the desired shape. This is a common technique for shape correction in AO [16].

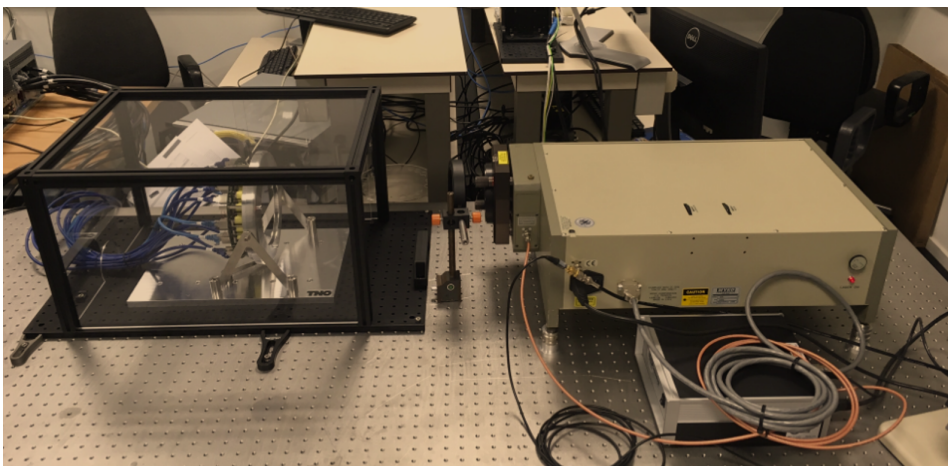


Figure 3.3: Test setup for measuring deformation of the deformable mirror facesheet (left) using an interferometer (right). Source: M.J. Baeten, TNO

Each of the Influence function images is a matrix $\gamma_i(x, y)$. The IF matrix can be vectorized into $\bar{\gamma}_i$ where

$\bar{\gamma}_i = \text{vec}(\gamma_i(x, y)) \quad \forall \quad \text{vec}: \mathbb{R}^{m \times n} \rightarrow \mathbb{R}^{mn}$. The combination of all IF's is formatted into an influence function matrix \mathbf{IF} in the following way:

$$\mathbf{IF} = [\bar{\gamma}_1 \dots \bar{\gamma}_{57}] \quad (3.1)$$

The mirror can deform and fit shapes using weighted values of the IFs: an objective shape $\theta(x, y)$ in vector form $\bar{\theta}$ may be fitted using the following expression:

$$\bar{\theta} = \frac{\bar{I}_\theta}{\bar{I}_n} \mathbf{IF} \quad (3.2)$$

In order to drive the mirror to a desired shape eq. 3.2 needs to be rearranged. \bar{I}_θ is the unknown and is taken to the LHS of the equation. This requires the use of a Least Square (LS) fit algorithm to transform matrix \mathbf{IF} which follows:

$$\bar{I}_\theta = (\mathbf{IF}^T \mathbf{IF})^{-1} \mathbf{IF}^T \bar{\theta} \quad (3.3)$$

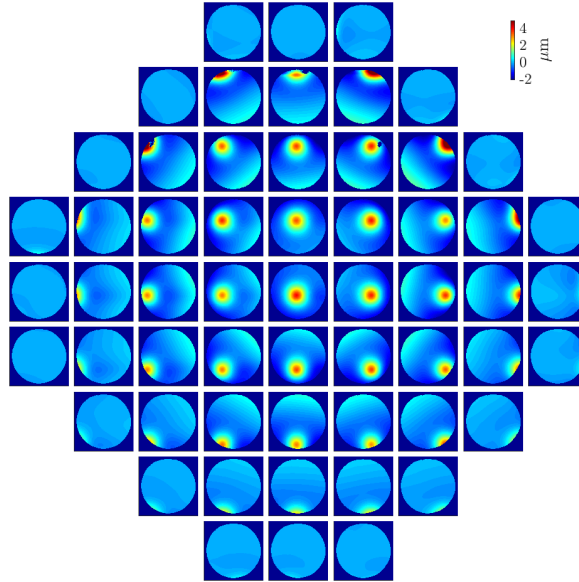


Figure 3.4: 57 individual Influence Functions measured with the interferometer. Each image constitutes one of the columns of the \mathbf{IF} matrix and is used in shape reconstruction algorithms.
Source: R. Saathof, TNO

Driving the currents of \bar{I}_θ to the DM will cause it to deform to the best fit of the desired shape. Reconstructed wavefronts can also be achieved numerically using the following:

$$\bar{\theta}_{reco} = \mathbf{IF} \bar{I}_\theta \quad (3.4)$$

This least square fit approach will be used to generate the objective shapes that the mirror facesheet must adopt.

3.3. ADVANTAGES AND CHALLENGES OF THE DEFORMABLE MIRROR

TNO has delivered a prototype of a deformable mirror which can achieve high stroke actuation with maximum accuracy. The light weight of the system makes it suitable for space applications. It also has low power consumption and is highly reliable. These features are promising towards a deformable mirror suited for most adaptive optics applications. The linear behavior of the actuators enables the desired open-loop capabilities required in state-of-the-art astronomical instruments (see section 5.2).

The DM design is also subject of improvements. Influence of non-identified errors was detected during the characterization of the flattening capabilities of the mirror. The best flat tests consist of lowering the surface error of the measured resting shape $\theta_0(x, y)$. This is achieved by supplying a set of currents \bar{I}_f that would result in a shape complementary to the resting shape $\theta'_0(x, y)$. The result should be a perfectly flat surface. However, it was seen that when iterating over the flattening algorithm (eq. 3.2), convergence to the best flat was reached after several iterations (Figure 3.6). Also, high amplitude bumps were detected in the mirror facesheet. This gave place to a high value of the Peak to Valley.

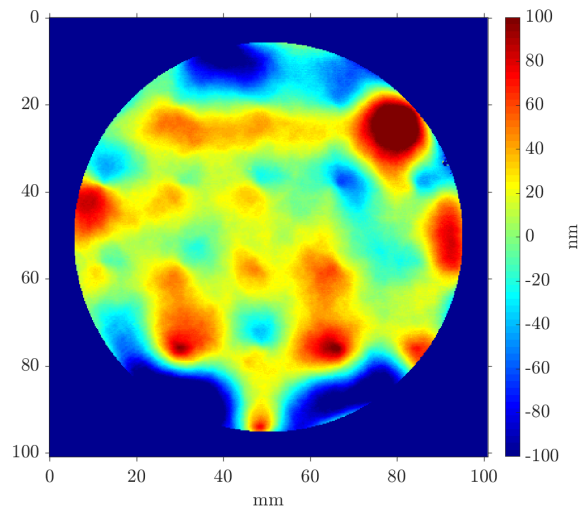


Figure 3.5: Interferometer image of the experimental best flat after six iterations in a control loop using algorithm described in section 3.2. Note the bump in the upper-right area. Source: M. Baeten, TNO

These unidentified behavior motivated the study of the system from a modeling point of view. By identifying the sources of the closed loop increase behavior it is expected to increase the shape reproduction capabilities of the mirror resulting in an even preciser DM.

Also, in order to further improve the performance of the DM, some mechanical parameters of the DM were tuned. This allowed to determine whether there exist design-parameter combinations for which the DM is more accurate. The mechanical parameters evaluated were: actuator layout, number of actuators, fill factor, stiffness of the actuators and thickness of the facesheet.

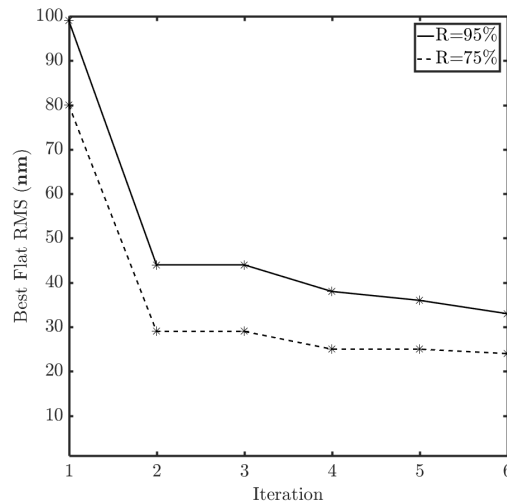


Figure 3.6: Evolution of the surface error RMS with flattening iterations for the mirror surface. Error decreases with every iteration of the control loop up to 6 iterations. *Source: M. Baeten, TNO*

Fill factor	P-V (nm)	RMS (nm)
95%	324	34
75%	167	25

Table 3.1: RMS and Peak-Valley values of the experimental Best Flat after six iterations using the control loop

3.4. RESEARCH QUESTIONS

Based on the background information given in this and the previous chapter, the following research questions were formulated:

- Is it possible to optimize the deformable mirror design in terms of the mechanical properties of its actuators and facesheet?
- Will the layout of actuators influence the performance of the deformable mirror?
- Is there a unique set of values of the mechanical properties of the actuators and mirror facesheet which globally maximizes the resolution of imaging while minimizing the power dissipation?
- Is the effect of actuator print-through dominant over the effect of the initial flat for the optical quality?

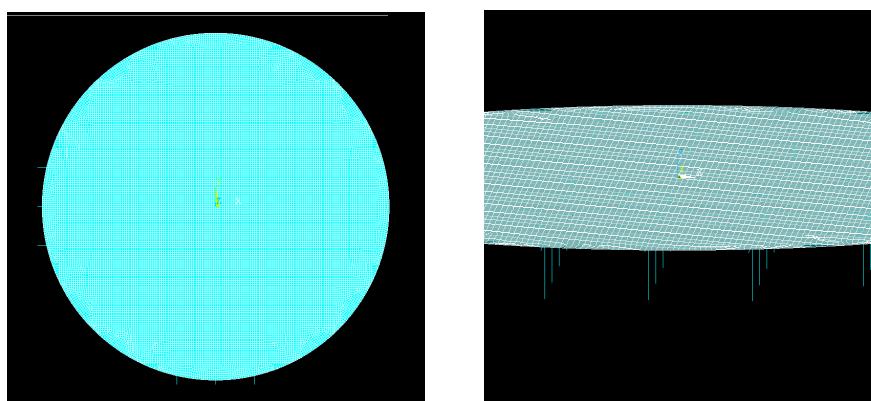
4

FINITE ELEMENT MODEL OF A DEFORMABLE MIRROR

This chapter describes two FEM models used for the analysis of the DM and its optimization. First, a 2D shell element model is presented. This model was validated using the interferometer images from figure 3.4. The model was used for the optimization shown in chapters 5 and 6. This chapter also presents a model incorporating the 3D surface of the resting shape of the mirror facesheet. It was used to investigate the influence of the mirror facesheet's resting shape in the optical quality of the DM's active flatness.

4.1. SHELL ELEMENT PARAMETRIC MODEL

The shell element model incorporates the mirror facesheet and the actuators. The facesheet is represented with 2D shell elements. The actuators are modeled as linear stiffness elements in the out-of-plane and in the in-plane directions. Each actuator has three stiffness elements: two in the in-plane directions and another in the out-of-plane direction. The stiffness elements constraint the model. They are elastically fixed in all three directions of space and have no rotational degrees of freedom. The element size is set to 1 mm.



(a) (b)

Figure 4.1: (a) Plant view of the 2D Shell element model used for parametric study and optimization.
(b) Detail of the same FEM model including view of actuators

The model's inputs are forces applied on the actuator nodes. The output of the simulations is a displacement field for the nodes of the facesheet. The strain formulation is logarithmic. The boundary conditions of the

model are free edge and the (elastically) fixed actuator supports. Therefore rigid body motion takes place. The actual DM prototype does have three leaf springs that further constraint the facesheet in the in-plane (and out-of-plane) direction. These are neglected in the model because only out-of-plane motion is measured. The FEM model is parametric. Its mechanical properties can be varied in iterative simulation loops. The location of the actuators can also be modified, as can be the number of actuators. Code with which to compute the simulations is shown in appendix D.

4.1.1. VALIDATION OF THE MODEL WITH EXPERIMENTAL DATA

The main objective of the model is to generate influence functions in physical accordance to those generated by the DM prototype. The approach is to modify mechanical parameters that influence the shape of the IFs from the model. Since the value of the stiffness of the actuator supports is unknown, it is chosen as the design variable over which to iterate.

Material Property	Symbol	Value	Units
Density	ρ	2328	kg m^{-3}
Modulus Of Elasticity	E	70	GPa
Poisson ratio	ν	0.3	-
Strut/Support Stiffness	k	-	N m^{-1}
Thickness of Mirror Facesheet	t	1	mm
Diameter of Mirror Facesheet	Φ	160	mm

Table 4.1: Table of material properties used in the model. Stiffness is undetermined

The validation is done by minimizing the residual error of the modeled IFs and the experimental IFs. The shape of the modeled IFs is modified in an iteration loop by changing the value of the actuator stiffness. Each iteration, the stiffness value of the supports is increased by $2 \times 10^3 \text{ N}$. An IF function with the same input parameters as those from the experiments is computed. Then this IF is subtracted from an experimental interferometer image. The result is a residual shape for which the

RMS error is computed. This measure of error is referred to as the surface error RMS:

$$RMS = \sqrt{\sum_{i=1}^N \frac{(r_i - f_i)^2}{N}} \quad (4.1)$$

Where r_i are the measured points from an interferometer IF (as those from figure 3.4), f_i are the modeled IF points and N is the number of analysis points in the mirror domain. The stiffness value for which the error is minimized will give the better fitting IFs.

The results of this analysis are shown in figure 4.4, which shows the surface error RMS for every simulated stiffness value. The process is repeated for two actuators: central actuator, and a non-centered actuator. The analysis is also performed for different actuation forces. The stiffness value for which the residual error is minimized is the same in all tests, there are variations however in the minimum surface error achieved. This may be explained by variations in signal to noise ratio, which changes with the supplied actuator force.

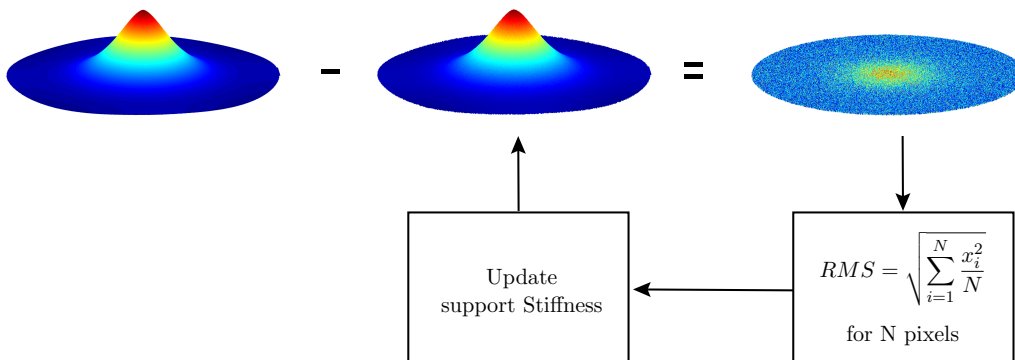


Figure 4.2: Schematic of the validation for stiffness of the supports using an iteration loop: subtract the experimental IF to a surface interpolated from FEM nodes. Compute RMS of residual and update stiffness. Then repeat the process

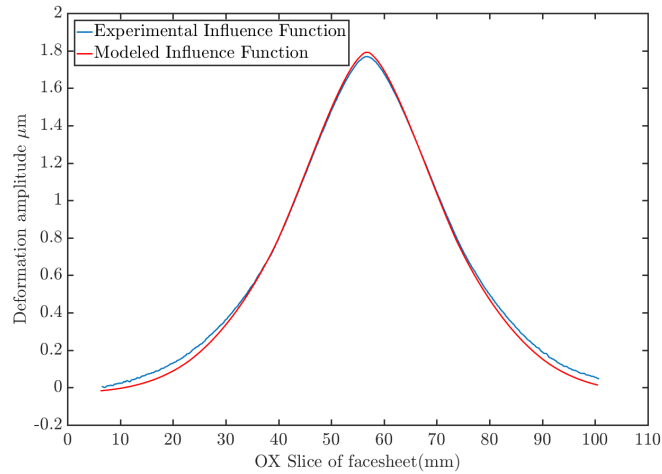


Figure 4.3: Slice through origin of the superposition of an experimental IF and a modeled IF

For the simulated stiffness values, there is a global minimum error for support stiffness $68 \times 10^3 \text{ N m}^{-1}$. The residual error at that point is approximately 99 nm. The error cannot be minimized further. Noise present in the measurement data and a small amount of piston limit the quality of the influence function fit. A cross cut of the superposition of a modeled IF and the experimental IF shows the noise present in the experimental data (figure 4.3).

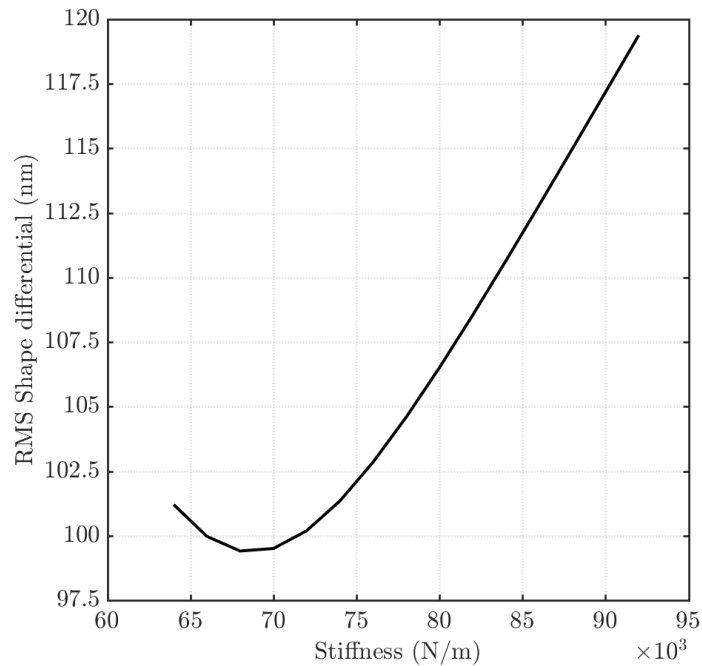


Figure 4.4: Graph comparing residual surface error of model and experimental images for different support stiffness values of the model. The most physical support stiffness value is found at the lowest point in the graph

4.2. 3D MODEL OF FACESHEET SURFACE

The 3D model reconstructs the resting shape of the mirror surface. The model is built to compare active flattening behavior of the actual prototype and a model where all variables are controlled. To obtain the

original resting shape of the DM, an interferometer image is used. The interferometer has an aperture of 107 mm diameter leaving the remaining mirror surface in the blind. In order to model the behavior facesheet, a full-size image of the resting shape is required. Otherwise, actuation in the blind area cannot be modeled. To overcome this limitation, the blind area of the mirror is extrapolated using a modal decomposition of the original interferometer image.

The extrapolation begins with the decomposition of the interferometer image into a set of regression variables. The regression variables are terms from a 2D Fourier series. The frequencies used for the extrapolation range from $0 \frac{\text{cycles}}{\text{meter}}$ to $3 \frac{\text{cycles}}{\text{meter}}$. Two regressors are needed for the process of the extrapolation: first, a regressor of the size of the interferometer image for obtaining the regression variables \mathbf{R}_{IF} . And another regressor of the size of the full mirror domain \mathbf{R}_{160} for the extrapolation. Both regressors have the same structure, only the amount of spatial points changes. The regressors and the regression procedure are:

$$\mathbf{R}_{\text{IF}} = \begin{bmatrix} 1 & \sin(2\pi f_1 x_1) & \cos(2\pi f_1 x_1) & \sin(2\pi f_1 x_1) \cos(2\pi f_1 x_1) & \sin^2(2\pi f_1 x_1) & \cos^2(2\pi f_1 x_1) & \dots \\ \vdots & \vdots & \vdots & \vdots & \vdots & \vdots & \vdots \\ 1 & \sin(2\pi f_1 x_n) & \cos(2\pi f_1 x_n) & \sin(2\pi f_1 x_n) \cos(2\pi f_1 x_n) & \sin^2(2\pi f_1 x_n) & \cos^2(2\pi f_1 x_n) & \dots \end{bmatrix} \quad (4.2)$$

where $n = a * b$, a and b are the total x and y analysis points, f_1 is the first frequency. The regression is formulated as:

$$\bar{m} = (\mathbf{R}_{\text{IF}}^t \mathbf{R}_{\text{IF}})^{-1} \bar{y} \quad (4.3)$$

Where \bar{y} is a vector containing the points from the interferometer resting shape (figure 4.5 (a)). Vector \bar{m} contains the regression variables. Note that the size of this vector is independent of the size of the domain. It can be used to reconstruct a bigger domain with the same frequency content. A virtual full surface is reconstructed using the regressor \mathbf{R}_{160} (which contains the domain points needed to reconstruct a $\varphi = 160$ mm domain):

$$\bar{\theta}_{xtr} = \mathbf{R}_{160} \bar{m} \quad (4.4)$$

The resulting vector $\bar{\theta}_{xtr}$ is the extrapolation vector which can be reshaped into a matrix $\theta_{xtr} = \text{vec}^{-1}(\bar{\theta}_{xtr}) \forall \text{vec}^{-1}: \mathbb{R}^{mn} \rightarrow \mathbb{R}^{m \times n}$ which is shown in figure 4.5 (b).

One of the limitations of the extrapolation procedure is that some amplitude values of the sinusoidal waves in the blind area are very high. For this reason, amplitude values are limited to $7 \mu\text{m}$. So all higher values are set to a constant value $\theta_{xtr}(x_i, y_i) > 7 \mu\text{m} \rightarrow \theta_{xtr}(x_i, y_i) = 7 \mu\text{m}$

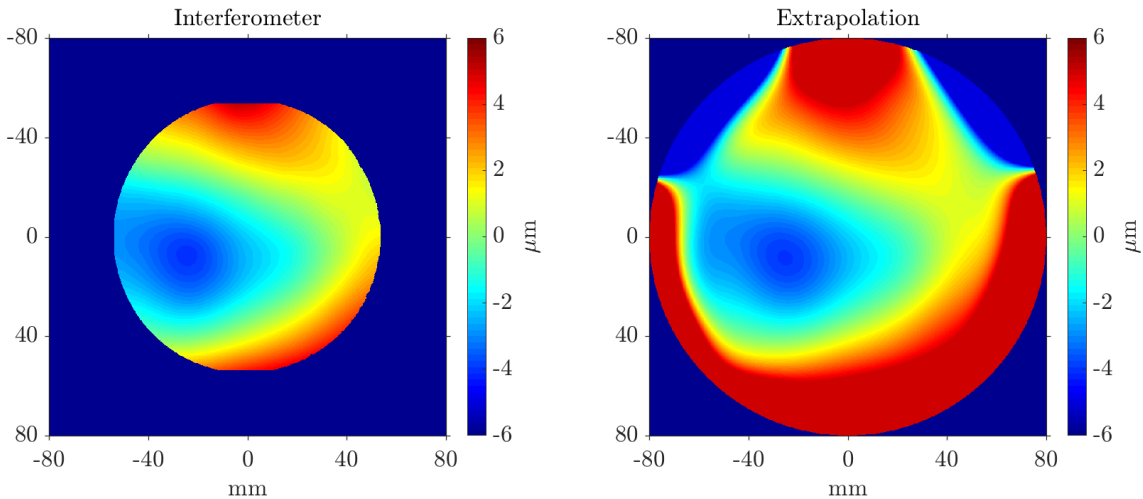


Figure 4.5: (a) Interferometer image of the resting shape of the DM. Aperture of the interferometer image is 107 mm (b) Extrapolation of the interferometer image over the full mirror domain

The extrapolated image is used to build a FE model. The image can be considered a cloud of points where pixel numbers and amplitude values are the coordinates. A surface is generated from the cloud of points and discretized to form a mesh of 3D brick elements using a FEM package. In the model, elastic foundation nodes are declared at the position of the actuators. The FEM model is linear and makes no further assumptions on constraints than those of the supports. For the simulation, forces are applied in the out-of-plane direction at each of the 57 groups of nodes contained within a circular area of diameter 1 mm set at the locations of the actuators. Further description of the interpolation and FEM model can be found in appendix C.

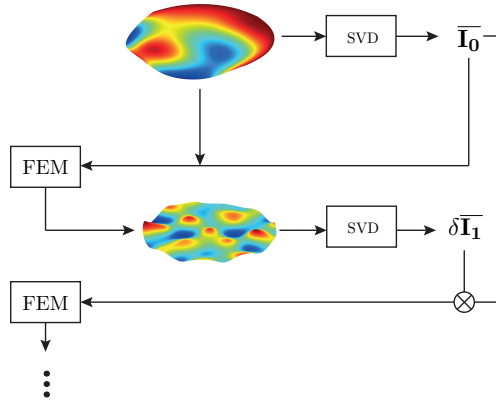


Figure 4.6: Flowchart of the modeled flattening procedure. The LS algorithm from section 3.2 is applied to the modeled facesheet to determine the best flat. The process is then repeated updating the currents to be supplied to the model

Once the model has been assembled, the closed-loop flattening procedure of the prototype is emulated. Since the surface outside of the interferometer area is virtual, it is masked during the procedure. The least square fits will only use information from the area of the interferometer aperture. To find the model's best flat, the same procedure as in section 3.2 is followed. The first step to take is to extract the 57 individual influence functions from the DM model: simulate a unit load at each actuator nodes location, interpolate a matrix, vectorize the matrix and store it as a column of a **IF** matrix. Then, using linear least squares and the shape of the model's surface, obtain a set of actuation commands $\bar{\mathbf{I}}_0$. These are the force inputs fed to the FEM routine when running a simulation (individual IFs from the model are measured with a force 1 N and therefore regression variables are forces). The resulting surface is again evaluated with the linear least squares algorithm. A new set of incremental force in-

puts is extracted. By adding these new $\delta\bar{\mathbf{I}}_1$ regression variables to the original set $\bar{\mathbf{I}}_0$, a new set of force inputs is obtained $\bar{\mathbf{I}}_1 = \bar{\mathbf{I}}_0 + \delta\bar{\mathbf{I}}_1$. This vector is used as an input for the FEM model. The process is repeated six times. At every iteration the peak-to-valley and the surface error are evaluated. It is observed that for the surface error, convergence is reached after three iterations. The Peak-to-Valley reaches its minimum value after four iterations (figure 4.7).

The results show a clear magnitude order difference between the model and the experimental results seen in section 3.3. Nevertheless, the optical quality does increase with the iterative procedure. This behavior is similar to that of the prototype.

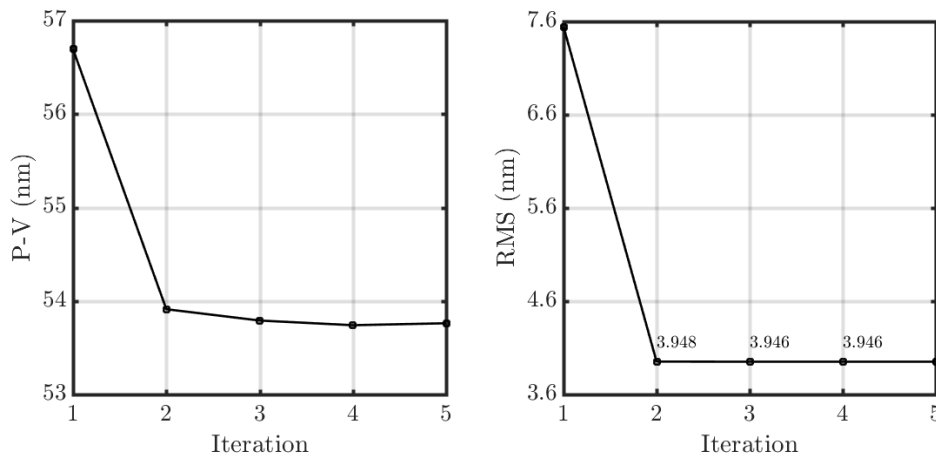


Figure 4.7: (a) Peak-Valley convergence in the 3D model of the resting surface of the DM. Convergence happens after 4 iterations (b) RMS convergence is reached in the third iteration

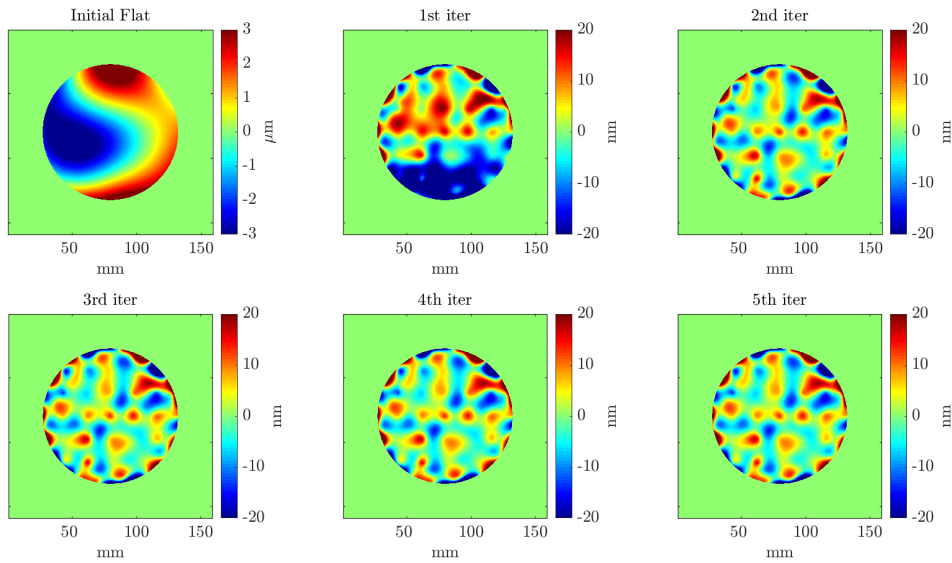


Figure 4.8: Evolution of modeled facesheet flatness with the best flat algorithm

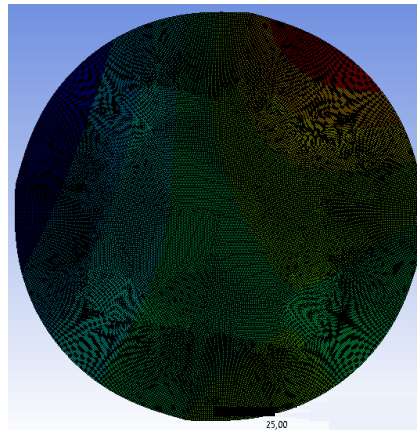


Figure 4.9: Caption of the 3D surface FEM model. Units mm

In this chapter two FE models have been presented. A 2D shell element model which can reproduce IFs which are previously validated. Validation is done through tuning of actuator stiffness. The residual error between modeled and experimental results is 90 nm RMS and is caused by noise and misalignment. Nevertheless, the global minimum coincides for several test cases. This model can be used to predict design sensitivities of the DM. A 3D model has also been shown to behave in a similar way to the DM prototype when applying active flattening algorithm. The same iterative convergence as in the DM prototype is observed for the model. However, there is an order of difference in the values of RMS and PV. Spatial information for the model is much more abundant and noise free, this explains the easiness of the algorithm to generate results.

5

DEFORMABLE MIRROR LAYOUT

This chapter presents the performance of different actuator layouts for atmospheric turbulence correction. The following are tested: geometrical dispositions of actuators, optical aperture values and the use of different number of actuators. In total three actuator layouts from literature are evaluated: circular, hexagonal and square (which is the current disposition of actuators). An objective function is defined for measuring the performance of the different layouts: a set of Fourier polynomials. These polynomials are compared to Zernike modes in the compensation of random atmospheric turbulence phase maps to prove that they are a better descriptor of atmospheric turbulence.

5.1. OPTICAL OBJECTIVE FUNCTION

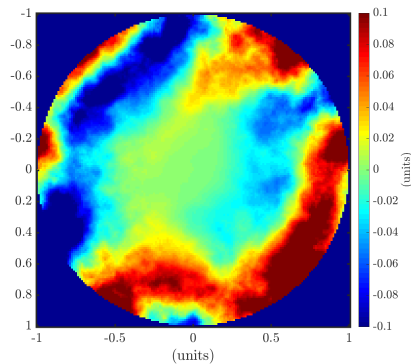


Figure 5.1: Random turbulence phase screen using Kolmogorov energy spectrum

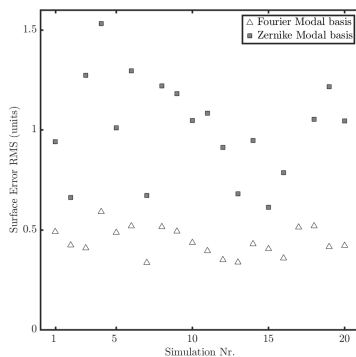


Figure 5.2: Surface error of a Fourier modal decomposition and a Zernike modal decomposition of 20 random phase screens

In order to determine which layout performs better for correcting atmospheric turbulence, a figure of merit needs to be defined. Fourier polynomials are chosen as the objective function for the optimization of the DM. Performance of the DM is measured as the resolution with which these modes can be corrected. Fourier modes are chosen as a modal basis because they compensate numerical turbulence images with a higher resolution than Zernike modes. In this thesis, turbulent images are generated using the Kolmogorov energy spectrum. The Kolmogorov Power Spectrum is in good agreement with experimental turbulence as mentioned by some authors [17] and it reads:

$$\Phi(f) = 0.023r_0^{-5/3} f^{-11/3} \quad (5.1)$$

By convoluting the Kolmogorov PSD with a domain conformed of random coefficients ranging 0 to 1, a finite random turbulence image is obtained. This can be done by applying a Fast Fourier Transform (and shifting to the center) to a matrix. The matrix being the point-wise multiplication of the PSD and the random-entry matrix \mathbf{R} . By taking the real part of this matrix, an image similar to figure 5.1 is obtained. The mathematical expression reads:

$$\mathbf{K} = \text{Re}(\Phi \otimes \mathbf{R}) \quad (5.2)$$

Where \mathbf{K} is the random Kolmogorov phase map and Φ the 2D PSD.

The Fourier modal basis is conformed of the terms of the Fourier series in two dimensions. A finite set of frequencies ranging from zero to the spatial Nyquist frequency of the actuators is chosen. The actuators are positioned with an 18 mm pitch. The Nyquist frequency is then $\frac{18}{2*1000} \text{ cycles/meter}$ which is rounded to 3 cycles/meter . The Fourier polynomial basis can be expressed as:

$$x_{ab,1} = \sum_{i=1}^a \sum_{j=1}^b \sin(2\pi f_{x_i} \bar{x}) \cos(2\pi f_{y_j} \bar{y}) \quad (5.3)$$

$$x_{ab,2} = \sum_{i=1}^a \sum_{j=1}^b \cos(2\pi f_{x_i} \bar{x}) \cos(2\pi f_{y_j} \bar{y}) \quad (5.4)$$

$$x_{ab,2} = \sum_{i=1}^a \sum_{j=1}^b \sin(2\pi f_{x_i} \bar{x}) \sin(2\pi f_{y_j} \bar{y}) \quad (5.5)$$

$\forall a, b = 0 \dots 3$ The modes sum up to 37. In the evaluated mirror designs only 25 of the modes are evaluated, since the rest are symmetric modes. The modal basis is referred to as \mathbf{F}_{25} .

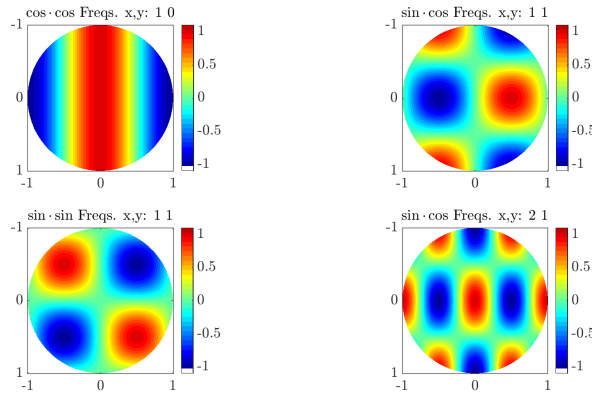


Figure 5.3: Some low order Fourier modes from the modal basis

The justification for the choice of the Fourier modal basis is that it compensates Kolmogorov phase maps (\mathbf{K}) with higher resolution. This is shown in figure 5.2, which is the result of a simulation comparing the resolution of Zernike modes and Fourier modes for several random \mathbf{K} matrices. Both modal bases are formed of by the 37 lowest terms of each series. A more extensive description of this validation can be found in appendix A.

5.2. LAYOUT STUDY AND FILL FACTOR

In order to test the influence of the actuator layout on the optical resolution for the objective function, three actuator layouts are compared. The chosen layouts are: square, circular and hexagonal. These layouts have been tested in literature previously for determining optimum layouts in Zernike mode correction [16] and other (see section).

The layouts are modeled using the FEM code from section 4.1. To generate the actuator patterns, the location of the stiffness supports is modified. The actuators layouts have a minimum pitch of 18 mm and they all have a central actuator. The geometrical distribution of the layout is built around the central actuator.

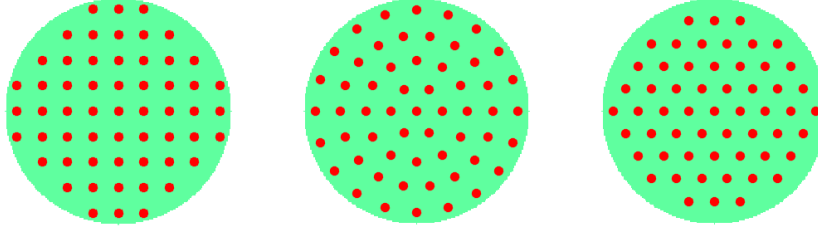


Figure 5.4: Tested actuator layouts: rectangular, circular and hexagonal. These layouts have been evaluated previously in literature for different figures of merit and applications

Optical resolution is measured following the procedure shown in section 3.2. To assemble the three \mathbf{IF} matrices: \mathbf{IF}_r , \mathbf{IF}_c and \mathbf{IF}_h . 57 individual simulations are carried out to extract individual IFs. The θ to be corrected are each of the Fourier polynomials conforming \mathbf{F}_{25} .

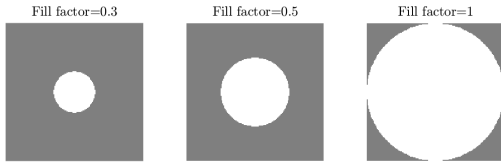


Figure 5.5: Fill factor changes the radius of the active optical surface and is defined as $ff = r_a/r_t$

The fill factor is tested simultaneously. Fill factor is defined the radius of the active surface for imaging. It is defined as: $ff = r_a/r_t$ where r_a is the active radius and r_t the total radius of the DM. Some authors have found that to achieve quality in the correction of low order Zernike modes, some actuators need to be placed outside of the field of view of the mirror [19]. The possibility of finding a reduced aperture at which resolution is optimized motivates the study of the fill factor. To this end, the correction of the individual Fourier modes is repeated in an iteration loop for varying fill factors. Every iteration quality of correction of the Fourier polynomials is evaluated at a different ff . This is done for fill factor values ranging from 0.1 to 1. Every iteration, the added surface error of the all corrected modes is computed in the following way:

$$\sigma_{ff,layout} = \sqrt{\sigma_{mode_1}^2 + \dots + \sigma_{mode_{25}}^2} \quad (5.6)$$

Where $\sigma_{ff,layout}$ is the added standard deviation (std) at a given layout and ff , and the terms correspond to the squared residual RMS of every mode correction. The values of $\sigma_{ff,layout}$ are plotted in figure 5.6.

The masks required to change the fill factor in the \mathbf{IF}_r , \mathbf{IF}_c and \mathbf{IF}_h matrices are boolean matrices for which the entries with $r > r_a$ are zero. The Fourier modes are generated every time over the surface prescribed for each ff as is shown in appendix A. Masks are defined as:

$$\delta(r) \begin{cases} \text{if } r < r_a & = 1 \\ \text{if } r > r_a & = 0 \end{cases} \quad (5.7)$$

Where r_a is varied every iteration. They are then vectorized into $\overline{mk} = \text{vec}(\delta(r))$. Also a matrix whose 57 columns are transposed vectors \overline{mk} is defined as:

$$\mathbf{M} = [\overline{mk} \dots \overline{mk}] \quad (5.8)$$

So that every iteration the trace of \mathbf{IF} and \mathbf{M} masks the domain to a desired radius:

$$\overline{I}_\theta = ((\mathbf{IF} : \mathbf{M})^T (\mathbf{IF} : \mathbf{M}))^{-1} (\mathbf{IF} : \mathbf{M})^T \overline{\theta} \quad (5.9)$$

$$\overline{\theta}_{reco} = (\mathbf{IF} : \mathbf{M}) \overline{I}_\theta \quad (5.10)$$

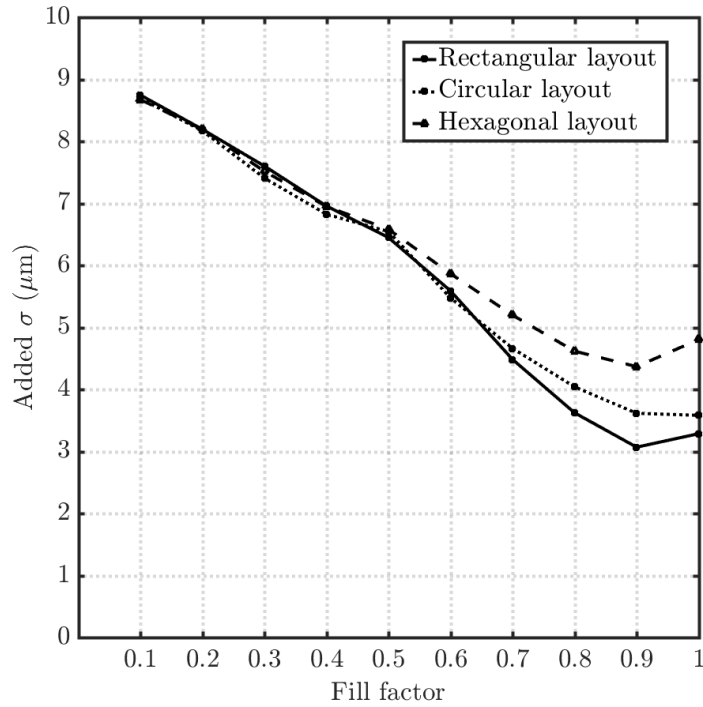


Figure 5.6: Added surface error of the three layouts for increasing Optical aperture. The lowest error is found for the rectangular layout at $ff = 0.9$

Figure 5.6 shows that for increasing fill factor the added surface error decreases for all layouts. The error decreases because exposing a higher number of actuators allows to reproduce higher order modes with more resolution. There is however an increase in the error when the full mirror is exposed ($ff = 1$) for the hexagonal and square layout mirrors. It arises from the fact that the hexagonal mirror and the circular mirror have no actuators close to the boundary.

It is also seen that the rectangular layout has a lower error than the circular and hexagonal layouts for $ff > 0.6$. This advantage is explained for the fill factor 0.9 with the fact that the actuators are arranged in a cartesian mesh. And so are the Fourier modes. However, in appendix B.2 it is shown that the layout of actuators does not have a significant impact on the quality of the correction, whereas ff does.

5.3. VARIATION OF NUMBER OF ACTUATORS

After choosing the square layout and $ff = 0.9$, the actuator pitch is varied. This results in different numbers of actuators in the DM surface. Actuators are added or lost in groups of 4. In this section, the effects on the optical quality are measured for different numbers of actuators. The approach is the same as in section 5.2. The numbers of actuators to be tested are: 69, 57 and 45. Their layout can be seen in figure 5.7.

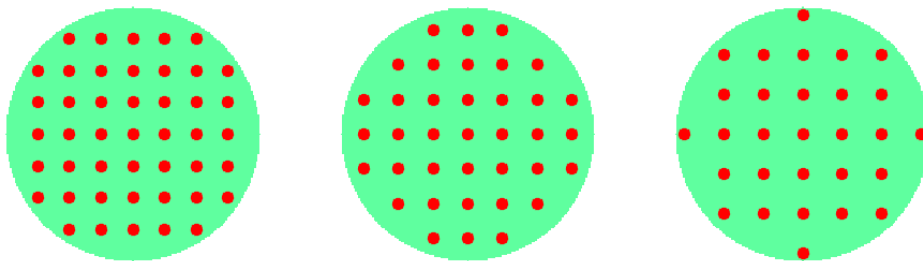


Figure 5.7: Mirrors with 69, 57 and 45 actuators (square arrangement). The change in optical quality is tested for these three cases

Figure 5.8 shows the surface error of the different actuator layouts for every simulated mode. Modes are

ordered in the following way: $\sin(2\pi f)\cos(2\pi f)$, $\sin(2\pi f)\sin(2\pi f)$, $\cos(2\pi f)\cos(2\pi f)$ for ascending frequencies f .

From figure 5.8 it is seen that although the error has a lower value of global error for the 69 actuator layout, the advantage is only given at the higher order modes. Lower order modes have similar error values for all layouts. The increase in resolution arising from increasing the number of actuators is small. The loss in resolution starts at a different mode for every amount of actuators.

Higher order modes, on the other hand, can only be described accurately by high actuation point count layouts. In the 69 and 57 actuator layout a wave-like variation is seen in the error. This variations have their origin in the spatial frequency match existing between the mode and the frequency of the actuators, which is similar in all cases.

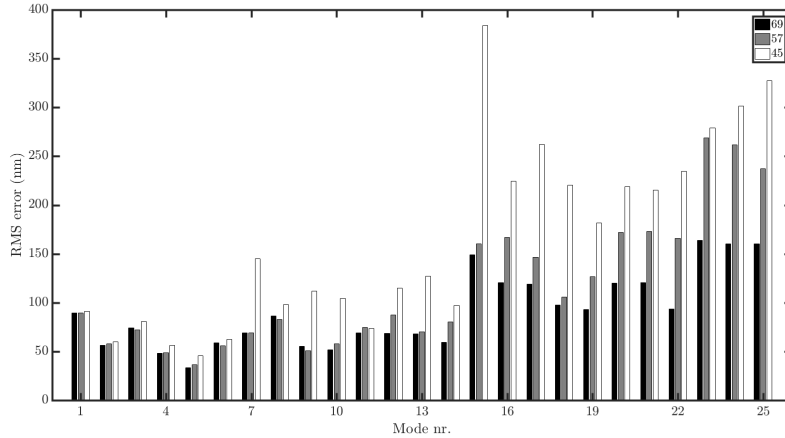


Figure 5.8: Surface error for actuator counts: 69, 57 and 45. The horizontal axes represents the modes ordered in ascending frequencies

In table 5.1 the lower order error is computed as $\sigma_{1-5} = \sqrt{\sum_{i=1}^5 \sigma_i^2}$ and is higher for the 69 actuators mirror. This is thought to be because of the implicit higher order stiffness that a higher number of actuators gives.

# Actuators	Actuator pitch mm	σ_{total} nm	$\sigma_{modes1-5}$ nm	$\sigma_{modes5-25}$ nm
69	16	494	142	473
57	18	672	142	657
45	19	948	154	936

Table 5.1: Standard deviation (RMS) of the different amounts of actuators for the correction of Fourier modes ranging 1 to 25

This chapter compares the optical performance of different actuator layouts and amounts of actuators. Before doing so it is shown that a set of Fourier polynomials is better suited for atmospheric turbulence compensations. These modes form a modal basis used as a figure of merit. It is shown that a square layout of actuators for a fill factor of 0.9/1 corrects the modal basis with a lower error than other evaluated layouts. It is also seen that increasing the number of actuators doesn't necessarily decrease the surface error. The 57 actuator layout shows better correction of lower order modes than the 69 actuator layout. It is also observed that lower actuator pitch values allow for correction of higher order Fourier modes.

6

DESIGN VARIABLES

In this chapter another approach for the optimization of the optical performance of DMs is presented. The approach is to tune the mechanical design variables of the DM. To that end, mirror thickness and actuator stiffness are tuned. Changes in optical performance are quantified for the aberration profiles described in section 5.1. A set of analytical expressions is extracted for some of the mechanical parameters. This chapter also presents a parameter study which compares the added surface error RMS of different combinations of mirror thickness and actuator stiffness values.

6.1. ANALYTICAL CURVES

To characterize the behavior of the DM under different design parameters, the following variables are studied: cross-coupling, amplitude of the surface deformation under a unit load and width of the influence function. All three variables are expressed as a function of the thickness of the mirror facesheet. In a separate analysis, the same is done for the stiffness of the actuator supports.

6.1.1. AMPLITUDE

Varying the stiffness of the actuator supports (k) and the mirror thickness (t) will modify the maximum deflection of the facesheet when a unit load is supplied to one of the actuators. The force required to displace the facesheet a prescribed distance is proportional to the power dissipated by the actuators; $P = IR^2$ and $F \propto I$. Therefore it is desired to maximize the amplitude of deformation when supplying a prescribed load.

To find the values of k and t that minimize power consumption, a parametric approach is used. Using the parametric shell element model from section 4.1, a unit load is provided as an input for one actuator. The deflection at the actuation point is measured. Then, t is varied and the maximum deflection results for varying t are expressed as a parametric curve. The same is done for k .

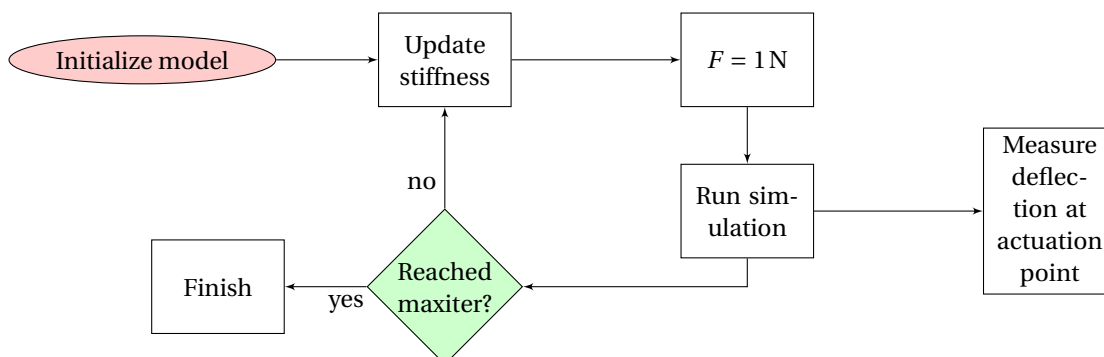


Figure 6.1: Flowchart for the simulations from this chapter.

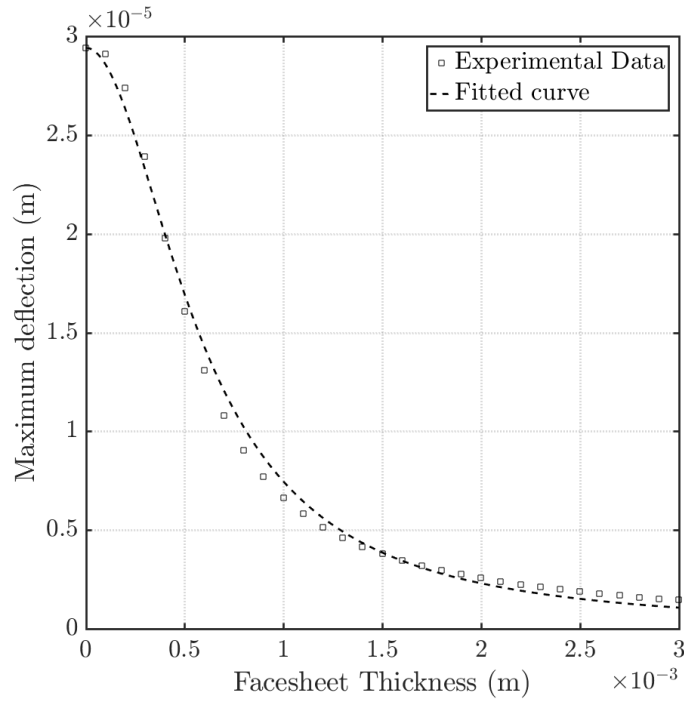


Figure 6.2: Experimental results and analytical curve for amplitude of facesheet deformation when varying thickness for a force input 1 N. Ideal power dissipation designs should have low facesheet thickness in order to maximize amplitude of deformation. Note the limiting maximum amplitude when thickness tends to 0

The results of modeling the deformation of the mirror facesheet under a unit load for different values of the mirror facesheet thickness are shown in figure 6.2. The figure also shows an equation fitted to the data. Fitting of the equation is done with MATLAB's fitting toolbox. The resulting fitted equation reads:

$$z = \frac{2}{6.8e4 + (2e11)t^3} \quad (6.1)$$

where z is the amplitude of the facesheet deformation at the actuator locations. The curve has an exponential decay caused by the increase in mirror thickness. Mirror thickness is a component of flexural rigidity. Increases in flexural rigidity naturally reduce maximum amplitude for a constant force. When values of t tend to zero, the maximum deflection reaches a limit value. This value corresponds to the elastic displacement of a spring with the same stiffness as the actuator support under the supplied load: $x = F/k$ where $F = 1$ N and $k = 68000$ N m⁻¹. The structure of the above equation is similar to that governing the bending of a plate resting on an elastic support. But this curve has an independent term that prevents the apparition of an asymptote when the thickness of the plate becomes very thin. A generic expression can be drawn:

$$z = \frac{F}{k + D} \quad (6.2)$$

Where F is the force supplied to an actuator and $D = \frac{Et^3}{12(1-\nu^2)}$ with E the Young's Modulus and ν the Poisson ratio.

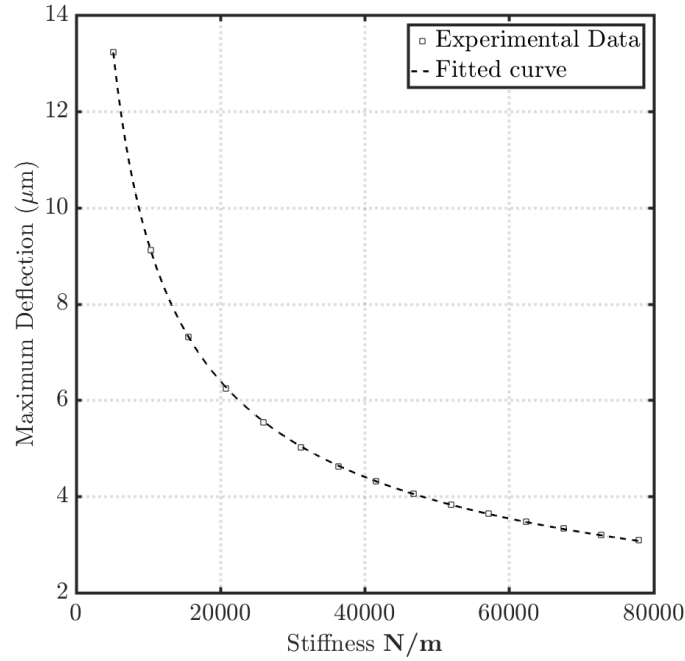


Figure 6.3: Relation between Amplitude of facesheet deformation for varying stiffness and a force input 1 N

The same approach is used for k . A curve is fitted to the modeled parameters to fit an equation that describes the behavior of the facesheet deformation under varying values of k . The results are shown in figure 6.3 showing the modeling points and a fitted equation which reads:

$$z = \frac{1326}{\sqrt{k}} \quad (6.3)$$

The curve from figure 6.3 shows how for small values of stiffness of the individual supports deflection tends to be infinite. When the stiffness values are high, deflection tends to zero. The higher the stiffness of the actuators, the higher the force needed to displace them. Thus, resulting in a lower facesheet deformation. The curve fit relates deflection and stiffness with a factor 2. This is thought to be caused by the combination of the actuator stiffness of several actuators in parallel, but no solid proof is found.

6.1.2. CROSS COUPLING

Cross coupling is defined as the displacement that an actuator experiences when a neighboring actuator is displaced. This phenomenon is said to smooth the shape of IFs as referred by [12]. Cross coupling can be expressed in the following manner:

$$xc = \frac{z_{adjacent}}{z_{actuated}} \cdot 100 \quad (6.4)$$

The influence of varying t and k on cross coupling when a constant load is applied is evaluated here. The variations are quantified using simulations. In a similar fashion to the previous section, parametric curves are obtained (measurements of displacement at and adjacent actuator are now needed as well):

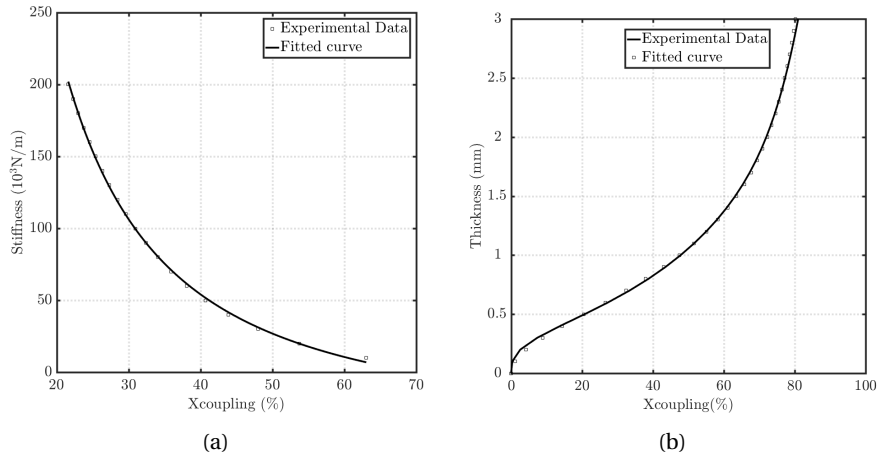


Figure 6.4: (a) Cross coupling variation for increasing stiffness of actuator supports (b) Cross coupling variation for increasing thickness

The curves can be fitted to analytic expressions as follows:

$$k = \frac{27350}{\sqrt{xc^3}} - 39.65 \quad (6.5)$$

In this case, the direct effect of the adjacent actuator has more weight, this changes the order of the equation for actuators influence the displacement

for k -Cross coupling relation. For t :

$$t = \frac{-103.1}{1.168 + t^{-1.954}} \equiv \frac{-103}{1 + t^{-2}} \quad (6.6)$$

The independent term from equation 6.5 represents the offset in the asymptote, k becomes zero before reaching 100 % cross coupling. On the other side of the graph, when cross coupling tends to zero, k becomes larger asymptotically. When cross coupling tends to 100 the stiffness value goes to zero. The second curve presents a similar behavior to eq. 6.1.

6.2. WIDTH OF THE INFLUENCE FUNCTION

Knowing the width of the IF is an interesting feature for modeling without having to use a FEM package. The width is considered as the radius from the actuation point to the point at which the facesheet crosses the mirror reference plane. Knowledge of this point and of the cross-coupling allows for the interpolation of a curve. The curve will range from the cross-coupled displacement, to the width and to the actuation point. Revolving the curve will give an IF. Another application for the width of the IF is to generate IF that match the actuator pitch. This application is interesting for piston generating mirrors, where the piston mode is wished to be optimized.

The analysis follows the same philosophy described in 6.1.1. Only that instead of measuring the maximum amplitude, the cross-points of the facesheet over the reference plane are measured. This is done using the code listed in annex E. When the IF generates a *sinc* shape, the zero-crossing happens at least twice. In that case, the crossing closest to the actuation point is measured. Equations with a physical relevance are not fitted to these parametric curves because of their high degree of non-linearity.

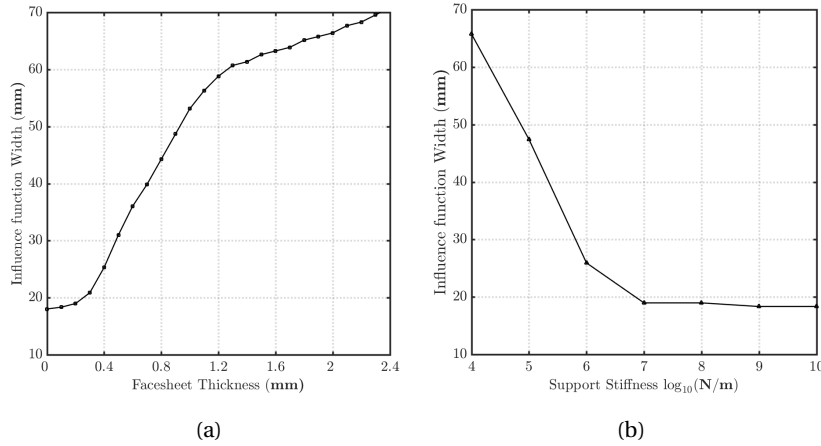


Figure 6.5: (a) Modeled thickness of the IF as a function of t . (b) Modeled thickness of the IF as a function of k .

In figure 6.5a three areas can be identified with three different slopes. The first section corresponds to IFs for which the width is smaller than the actuator pitch. The second area is that where the width of the IF is contained within the first and the second actuator. Finally, in the third section, the width is higher than the distance between three consecutive actuators.

The curve from 6.5b has a more stable relation since cross coupling is limited by increasing stiffness.

6.3. PARAMETER STUDY

The parameter study consists of combinations of values of t , k and the error of compensating for the Fourier modal basis shown in section 5.1. This is achieved by iterating over values of t and k and repeating the fitting procedure shown in section 3.2. It requires the coupling of the FEM model and MATLAB. The process consists of updating t and k every iteration and extracting the Influence functions. Using the SVD algorithm the full set of modes is fitted and the error quantified. Thickness values ranging from 0.1 mm to 2 mm are simulated. For stiffness the range is $1 \times 10^4 \text{ N m}^{-1}$ to $1 \times 10^7 \text{ N m}^{-1}$.

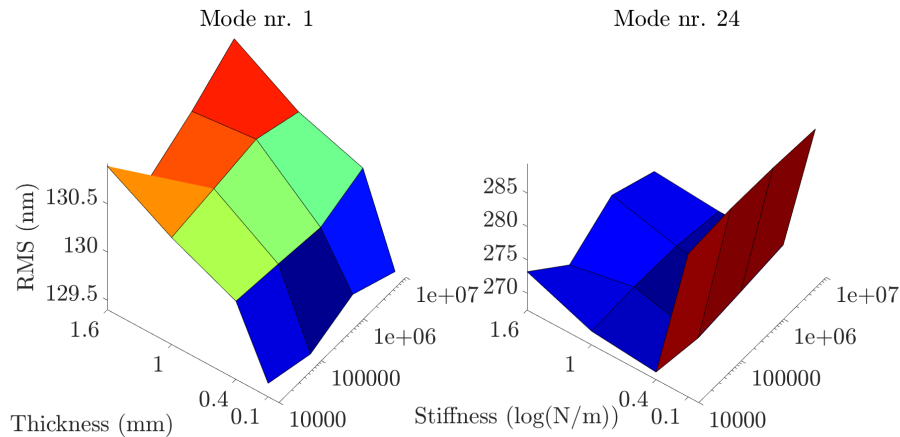


Figure 6.6: Constant shape of Influence function for varying stiffness(k), thickness(t) and Actuator spacing or pitch(p)

Figure 6.6 shows the error when correcting two different modes for a full set of combinations of t and k . Every mode has a different optimal configuration that minimizes the error. The global error is the added standard deviation of all error modes: $\sigma_{total} = \sqrt{\sum \sigma_i^2}$ for $i = 25$ modes. The addition of the errors gives place to a combined design space which is represented in figure 6.7.

In figure 6.7 a global minimum is found for the Standard Deviation of all modes used in this study. The minimum value of the added RMS error for all modes takes place for $t = 0.4$ mm and $k = 100 \times 10^3 \text{ N m}^{-1}$. These values of k and t are located towards the where the facesheet deformation tends to be higher (6.1.1).

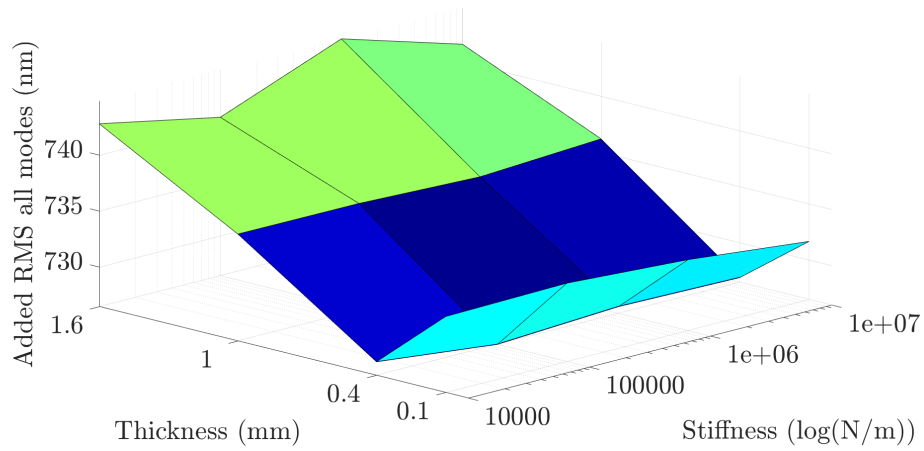
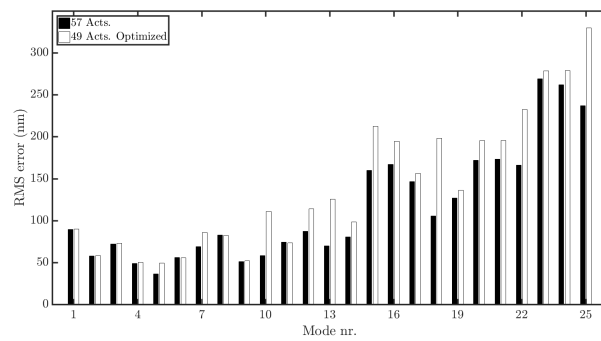


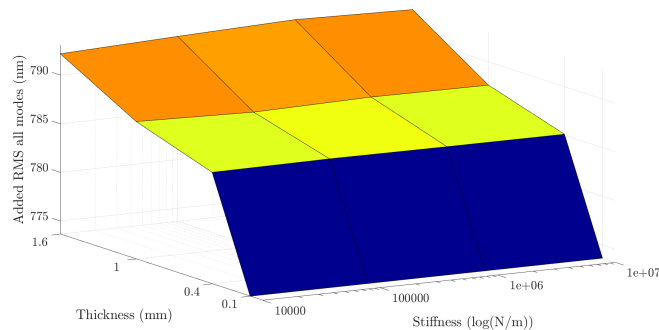
Figure 6.7: Combined design space: t, k, σ

6.3.1. PARAMETER STUDY FOR 49 ACTUATORS LAYOUT

Repeating the same process for the 49 Actuator layout will give an more resolute version of this layout making it able to generate modes with a resolution close to that of the higher count mirror. Looking at the minimum part of the design space and choosing those parameters. Their performance is compared to that of the original assembly.



(a)



(b)

Figure 6.8: (a) Error per mode for initial 57 actuator layout and optimized 49 actuator layout. (b) Design space for optimized 49

# Actuators	σ	$\sigma_{modes1-5}$	$\sigma_{modes5-25}$	Units
57	672	142	657	nm
49	811	147	797	nm

Table 6.1: Standard deviation (RMS) of the original and modified layouts

The described analytic curves in this chapter are an interesting tool for design optimization purposes. They can be inputted in optimization procedures to determine desired designs. The parameter study, on the other hand shows which values of mirror thickness and support stiffness give the global minimum error for the current load case.

7

CONCLUSIONS

The main objectives of this thesis were: to define whether optimal combinations of design parameters exist to increase the performance of the deformable mirror. And to determine whether the effect of the resting geometry of the facesheet surface is dominant in limiting the optical quality of the best flat. The conclusions chapter summarizes the interpretation of the findings of previous chapters. Recommendations are given based on the conclusions.

7.1. CONCLUSIONS FROM THE 2D MODEL

The 2D model is validated. The resemblance of the IF of the 2D model and the measured interferometer images has a minimum surface RMS value which is conditioned by the noise present in the interferometer images. A stiffness value of 68000 N m^{-1} is found to be the physical value of the stiffness of the supports. This value is in accordance with the combined stiffness of the actuator support and actuator strut. The 2D model can be used for modeling purposes, to explore the sensitivities of design parameters and to predict the behavior of alternative DM designs.

7.2. CONCLUSIONS FROM THE 3D MODEL

For the 3D model of the initial resting surface, three iterations are needed to converge to the best flat. This is modeled using the LS algorithm as was done with the DM prototype. The closed-loop convergence is caused by the geometrical non-linearity of the mirror surface. It is what prevents the mirror from reaching the best flat in open loop. There is a difference in the number of iterations needed to converge to best flat between model and real system (three against six of the prototype). There is also an order of magnitude difference in the surface error RMS (3.9 nm of the model and the surface error rms of the prototype 34 nm). The peak to valley values also differ: 54 nm for the model and 324 nm for the prototype. An influential factor explaining order of difference between model and prototype is the noise present in the measurement images. This noise affects the maximum resolution that can be achieved by the algorithm. Some similarities can be seen in the model best flat and the experimental case. Particularly the higher amplitude bump in the upper left corner of the 5th iteration from the model (Figure 4.8) and the experiments (Figure 3.5). This similarity further supports the hypothesis of the geometry being the main limitation for the best flat.

7.3. CONCLUSIONS FROM THE MIRROR LAYOUT

The figure of merit used in the optimization of the design variables was a set of Fourier polynomials (see section 5.1). Test results show that the set of Fourier modes are a more accurate basis for describing atmospheric turbulence (considered as random Kolmogorov phasemaps) than Zernike modes (see section 5.2).

The geometrical layout study involved a circular, rectangular and a hexagonal layout. In correcting Fourier modes the rectangular layout has a lower surface error. This holds for varying fill factor values. It was also shown that the fill factor corresponding to the lowest surface error is 0.9 for the square layout (see section 5.6). This is a result of having more actuators exposed to the active area. More actuators allow for the correction of higher order modes. The loss in precision for the full exposure is thought to be caused by the lack of actuators

in most of the outer ring. However, it is seen that no actuators need to be placed out of the aperture to increase optical quality. The reason being that Fourier modes satisfy the plate equation. The circular layout does experience further decrease in error in the case of full active area of the mirror surface. This is thought to be because of the more homogeneous distribution of actuators in the outer-most ring.

Varying the number of actuators has different effects on different sets of modes. For lower order modes it was expected to see a decrease in error for increasing actuator count. However, for low order modes, this decrease is negligible. For higher order modes, the results are as expected and quantified. Higher actuator count results in higher resolution in the reproduction of higher order modes.

7.4. MECHANICAL PROPERTIES OF THE MIRROR FACESHEET AND ACTUATORS

A set of analytical relations is set relating stiffness of the actuator supports and the mirror thickness with some variables of interest: deflection under unit load, Cross coupling and width of the influence function (eqs: 6.1, 6.1.1, 6.5). The stiffness of the supports can be tuned in terms of the geometry of the actuator strut and actuation beam or the material properties of the actuator. The facesheet bending can be tuned in terms of the material properties or its thickness. An interesting conclusion from figure 6.8b is that the output from the FEM model is physical but differs slightly from the theory of plates. In that solution to the bi-harmonic equation, the amplitude values tend to infinity.

From the parameter study it is concluded that there is a set of optimal values of the mechanical parameters of the facesheet and actuator supports that optimizes the optical performance of the DM. However, the increase in performance is limited (from σ_{added} 735 nm to σ_{added} 725 nm). Also, gravitational sag needs to be taken into account during that optimization.

7.5. RECOMMENDATIONS AND FUTURE WORK

The quality of the measured IFs has an effect on the degree of flatness that can be achieved in active flattening (see sections 3.2 and 4.2). Therefore, the use of an even more resolute interferometer could increase the quality of the best flat. Filtering the high frequency noise present in the images is another recommendation to this respect. The image noise affects the performance of the least square algorithm. Another factor influencing the quality of the best flat and the linearity of the facesheet displacement is the mirror surface. Using a facesheet with a higher degree of polishing (lower peak to valley in the resting shape) will help buffer the non-linear flattening effects seen in section 3.2.

It has been seen that the layout of the actuators does not influence the optical quality compared to other variables in the compensation of atmospheric turbulence. Therefore it is not recommended to change the current layout. For increase in optical quality, a higher number of actuators can be used as is mentioned in literature [11]. This of course results in a tradeoff between price and resolution. Furthermore, the increase in resolution is not substantial and for some modes there is even a loss in resolution (see table 5.1). The optical aperture on the other hand does have a stronger influence on resolution. It is recommended to increase to 90% of the total radius for optimal performance (see section 5.2). If it is desired to reduce the number of actuators, optimization techniques like the one described in section 6.3 will help buffer the decrease in optical resolution.

The parametric relations described in chapter 6 for the Influence functions allow to design DMs knowing before hand what the deformation behavior will be like. This relations can be fed to a FEM code or to a parametric model to quickly design and prototype different IF shapes. An interesting application of this feature is the optimization of specific aberration profiles such as those that need to be compensated in lithography or ophthalmology.

BIBLIOGRAPHY

- [1] R. Foy and F. C. Foy, eds., *NATO ASIB Proc. 198: Optics in astrophysics* (2005).
- [2] F. Roddier, *Adaptive optics in astronomy* (Cambridge University Press, The Edinburgh Building, Cambridge CB2 2RU, UK, 1999).
- [3] P. Wizinowich, *Adaptive optics in astronomy*, *Contemporary Physics* **56**, 432 (2015).
- [4] P.-Y. Madec, *Overview of deformable mirror technologies for adaptive optics and astronomy*, , 844705 (2012).
- [5] P. Hickson, *Atmospheric and adaptive optics*, *The Astronomy and Astrophysics Review* **22**, 76 (2014).
- [6] C. Li, M. Xia, Q. Mu, B. Jiang, L. Xuan, and Z. Cao, *High-precision open-loop adaptive optics system based on LC-SLM*, *Optics Express* **17**, 10774 (2009).
- [7] N. Devaney, E. Dalimier, T. Farrell, D. Coburn, R. Mackey, D. Mackey, F. Laurent, E. Daly, and C. Dainty, *Correction of ocular and atmospheric wavefronts: a comparison of the performance of various deformable mirrors*, *Applied optics* **47** (2008).
- [8] H. Kaushal and G. Kaddoum, *Optical Communication in Space: Challenges and Mitigation Techniques*, *IEEE Communications Surveys & Tutorials* **19**, 57 (2017).
- [9] R. Saathof, G. J. M. Schutten, J. W. Spronck, and R. H. Munnig Schmidt, *Actuation profiles to form Zernike shapes with a thermal active mirror*, *Optics Letters* **40**, 205 (2015).
- [10] A. Belmonte, M. T. Taylor, L. Hollberg, J. M. Kahn, L. C. Sinclair, F. R. Giorgetta, W. C. Swann, E. Baumann, I. Coddington, N. R. Newbury, J.-d. Deschênes, H. Bergeron, and M. Cermak, *Effect of atmospheric anisoplanatism on earth-to-satellite time transfer over laser communication links " Optical phase noise from atmospheric fluctuations and its impact on optical time-frequency transfer*, *Nat. Photonics Opt. Lett. Metrologia Nat. Photonics Phys. Rev. A* **16**, 471 (2015).
- [11] F. R. Rigaut, E. Ellerbroek, B., *Principles, limitations, and performance of multiconjugate adaptive optics*, *International Society for Optics and Photonics* **4007**, 1022 (2000).
- [12] R. F. M. M. Hamelinck, *Adaptive deformable mirror based on electromagnetic actuators*, Ph.D. thesis, Technische Universiteit Eindhoven (2010).
- [13] J. W. Evans, R. J. Zawadzki, S. M. Jones, S. S. Olivier, and J. S. Werner, *Error budget analysis for an adaptive optics optical coherence tomography system*. *Optics express* **17**, 13768 (2009).
- [14] E. Laag, D. Gavel, and M. Ammons, *Open-Loop Woofer-Tweeter Control on the LAO Multi-Conjugate Adaptive Optics Testbed*, *ArXiv*, 5 (2007), arXiv:0710.0405.
- [15] D. Mawet, *Adaptive optics i: principles, wavefront sensors, deformable mirrors*, http://www.astro.caltech.edu/~dmawet/teaching/ay122a_adaptiveoptics_1.pdf, accessed: 2017-09-30.
- [16] S. Verpoort and U. Wittrock, *Actuator patterns for unimorph and bimorph deformable mirrors*, *Appl. Opt.* **49**, G37 (2010).
- [17] M. Loktev, D. W. De Lima Monteiro, and G. Vdovin, *Comparison study of the performance of piston, thin plate and membrane mirrors for correction of turbulence-induced phase distortions*, *Optics Communications* **192**, 91 (2001).
- [18] M. Laslandes, K. Patterson, and S. Pellegrino, *Optimized actuators for ultrathin deformable primary mirrors*. *Applied optics* **54**, 4937 (2015).

- [19] G. Vdovin, O. Soloviev, A. Samokhin, and M. Loktev, *Correction of low order aberrations using continuous deformable mirrors*. *Optics express* **16**, 2859 (2008).
- [20] M. W. Smith and D. W. Miller, *Minimizing actuator-induced errors in active space telescope mirrors*, (2010) p. 773122.
- [21] H. Wang, *Research on a bimorph piezoelectric deformable mirror for adaptive optics in optical telescope*, *Optics Express* **25**, 8115 (2017).
- [22] G. J. Michels and V. L. Genberg, *Design optimization of actively controlled optics*, in *SPIE Proceedings Vol. 4198*, edited by M. A. Kahan (SPIE, 2001) pp. 158–162.
- [23] G. J. Michels, V. L. Genberg, K. B. Doyle, and G. R. Bisson, *Design optimization of actuator layouts of adaptive optics using a genetic algorithm*, , 58770L (2005).
- [24] S. Kuiper and N. Doelman, *Electromagnetic Deformable Mirror For Space Applications*, ICSO Conference, France 2016 (2016).
- [25] A. Rozene, *Characterization of Deformable Mirror for Adaptive Optics System*, Tech. Rep. (TNO, Delft, 2017).
- [26] G. Arfken, *Mathematical Methods for Physicists* (Academic Press, Orlando, FL, 1985).
- [27] S. W. Smith, *The Scientist and Engineer's Guide to Digital Signal Processing* (California Technical Publishing, www.DSPguide.com, 1998).
- [28] S. N. Bezdidko, *The Use of Zernike Polynomials in Optics*, *J. Opt. Techn.* **425** (1974).
- [29] R. Hoogeboom, *Optimization of the E-ELT M1 segment support locations*, Tech. Rep. (TNO, Delft, 2014).

A

2D FOURIER MODAL BASIS

This chapter describes the full set of Fourier polynomials to be used as both a modal basis for atmospheric turbulence representation and as an objective function for the different optimization procedures in chapters 5 and 6.

A.1. FOURIER POLYNOMIALS

Fourier series describe functions in terms of infinite sums of sines and cosines. The orthogonality of the sine and cosine functions allows for the construction of the Fourier series. The terms of a Fourier series can later be solved individually (decoupling). The linear addition of the terms then gives place to the original function [26].

The Fourier series can be generalized to the n-dimensional case. In this document the 2-D generalization is used. A finite Fourier series gives place to an approximation of the function that is desired to be reconstructed. The infinite full 2D Fourier expansion in 2D reads:

$$f(x, y) = \sum_{n=0}^{\infty} \sum_{m=0}^{\infty} \alpha_{n,m} \cos\left(\frac{2\pi nx}{a}\right) \cos\left(\frac{2\pi my}{b}\right) + \sum_{n=0}^{\infty} \sum_{m=0}^{\infty} \beta_{n,m} \sin\left(\frac{2\pi nx}{a}\right) \cos\left(\frac{2\pi my}{b}\right) + \sum_{n=0}^{\infty} \sum_{m=0}^{\infty} \gamma_{n,m} \cos\left(\frac{2\pi nx}{a}\right) \sin\left(\frac{2\pi my}{b}\right) + \sum_{n=0}^{\infty} \sum_{m=0}^{\infty} \delta_{n,m} \sin\left(\frac{2\pi nx}{a}\right) \sin\left(\frac{2\pi my}{b}\right) \quad (\text{A.1})$$

Where $0 \leq x \leq a, 0 \leq y \leq b$, n, m are frequencies in the OX, OY directions and $\alpha, \beta, \delta, \gamma$ are coefficients obtained through the orthogonality argument (weights).

This thesis uses each of the individual sine and cosine polynomials of a finite Fourier series -each term of equation A.1- as a term for a modal basis. The modal Fourier basis is used for decomposing atmospheric turbulence. They are also the figure of merit for the optimization process, since atmospheric turbulence is random.

The Fourier frequencies are limited by the design of the DM. Spatial frequencies are the variable of interest. There is a limitation to the highest achievable frequency by the DM imposed by the Nyquist frequency. The limiting DM parameter is actuator pitch which is set to 18 mm. And the Nyquist frequency [27]: $f_{nyq} = \frac{1}{2} \frac{160}{18} = 4.4 \equiv 4 \text{ cycle/meter}$

However, since any Optical aperture smaller than 90% will impede achieving the Nyquist Frequency, instead the maximum frequency considered is 3 cycle/meter. Also, The second and third terms of equation A.1 are symmetric with respect to the cartesian axis (and so are the evaluated layouts). Therefore the third term of equation A.1 is suppressed. Leaving the following modes:

$$\begin{aligned}
 f(x, y) = & \sum_{n=0}^3 \sum_{m=0}^3 \alpha_{n,m} \cos\left(\frac{2\pi nx}{a}\right) \cos\left(\frac{2\pi my}{b}\right) + \sum_{n=0}^3 \sum_{m=0}^3 \beta_{n,m} \sin\left(\frac{2\pi nx}{a}\right) \cos\left(\frac{2\pi my}{b}\right) \\
 & + \sum_{n=0}^3 \sum_{m=0}^3 \delta_{n,m} \sin\left(\frac{2\pi nx}{a}\right) \sin\left(\frac{2\pi my}{b}\right)
 \end{aligned}
 \tag{A.2}$$

Which, over a normalized circular aperture of radius 1 unit ($a = b = 1$) have the following graphical interpretation:

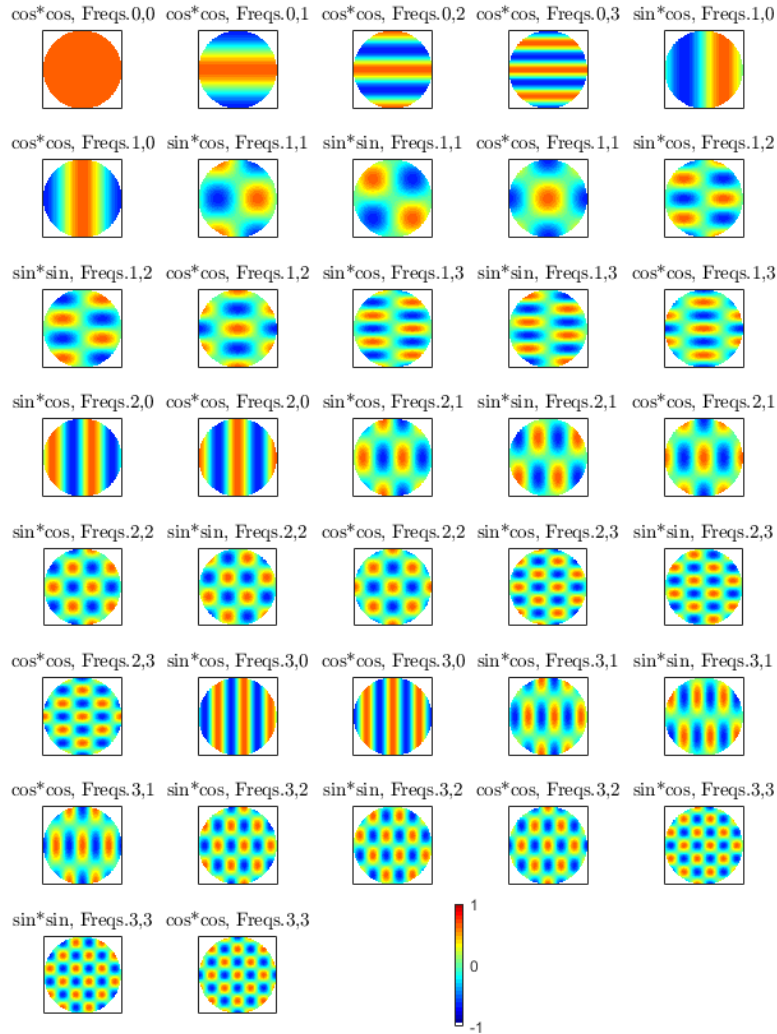


Figure A.1: Fourier polynomial Modes used for the modal basis. Frequencies range from 0 to 3 and the domain is made circular and normalized. Note that modes with mirrored frequencies are symmetric. Subtraction of these modes reduces the basis to 25 figures of merit. Piston should be present thrice but is only showed once

A.2. PERFORMANCE COMPARISON OF THE FOURIER SET AND THE ZERNIKE SET

Next step to take is to compare the resolution of a set of Zernike modes in the reconstruction of atmospheric turbulence; following the modal approach [9].

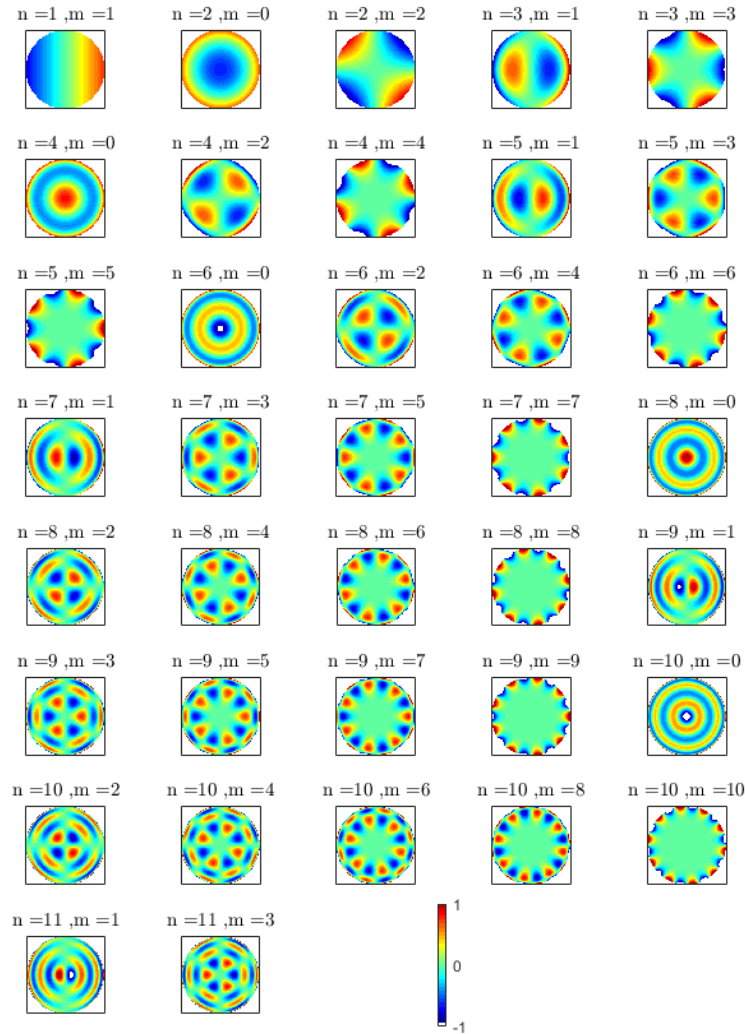


Figure A.2: Zernike polynomials (sine modes only) up to 37. These will be compared with Fourier modes to measure the accuracy of Atmospheric image modal decomposition

The same number of modes will be used as in the previous chapter A.1. The spatial frequency content will be different for the Zernike modes than for the Fourier modes. Zernike modes (Z_n^m) are derived from the following equations:

$$Z_n^m(\rho, \phi) = R_n^m(\rho) \cos(m\phi) \quad (\text{A.3})$$

$$Z_n^m(\rho, \phi) = R_n^m(\rho) \sin(m\phi) \quad (\text{A.4})$$

(for odd and even modes). The order of the polynomial is given by n and m which obey $n \geq m \geq 0$ and $R_n^m(\rho)$:

$$R_n^m(\rho) = \sum_{l=0}^{(n-m)/2} \frac{-1^l (n-l)!}{l! \left[\frac{1}{2}(n+m)-l\right]! \left[\frac{1}{2}(n-m)-l\right]!} \rho^{n-2l} \quad (\text{A.5})$$

More on Zernike modes can be found in [28]. The lowest 37 Zernike modes are shown in Figure A.2.

The generation of Atmospheric turbulence images was already described in 5.1. The code needed to generate this images reads:

```
sz=327; % size
cx=(-sz:sz); % Domain
mx=(ones(2*sz+1,1)*cx).^2;
mr=sqrt(mx+transpose(mx));
psd=0.023*mr.^(-11/3); % Kolmogorov PSD
psd(sz+1,sz+1)=0;
% generate the random numbers with Gaussian statistics
randomcoeffs=randn(2*sz+1)+i*randn(2*sz+1);
phasescreen=real(fft2(fftshift(sqrt(psd).*randomcoeffs))); % Convolute
% Make a circle in domain
phasescreen = disk_suppress(phasescreen);
phasescreen = 10e-6.*phasescreen; % Scale to um
```

The simulation consists in generating a number of random phase screens (100). For each simulation, the phase screen image is decomposed into the modal set of Zernike modes and into the modal set of Fourier modes \mathbf{Z}_{37} and \mathbf{F}_{37} respectively. Then the turbulence images are reconstructed using the coefficients from the decomposition and the modes. The reconstructed phasescreens are subtracted to the original phase screen and the surface error is computed. The result is a residual error per iteration which is plotted in figure A.3. The mathematical description of the method follows the same approach as 3.2 and can be written as:

$$\bar{\mathbf{Z}}_{reg} = (\mathbf{Z}_{37}^T \mathbf{Z}_{37}) \mathbf{Z}_{37}^T \bar{\mathbf{K}} \quad ; \quad \bar{\mathbf{K}}_{zern} = \mathbf{Z}_{37} \bar{\mathbf{Z}}_{reg} \quad (\text{A.6})$$

for the Zernike modal basis. The same principle is applied to for the Fourier basis. Then, the standard deviation of the residual is computed: $\sigma_{zern}(\bar{\mathbf{K}} - \bar{\mathbf{K}}_{zern})$ and $\sigma_{four}(\bar{\mathbf{K}} - \bar{\mathbf{K}}_{four})$. It is seen that for every generated random phase map, the error is always bigger for the Zernike basis. This justifies the choice of the Fourier basis as a figure of merit for the optimization.

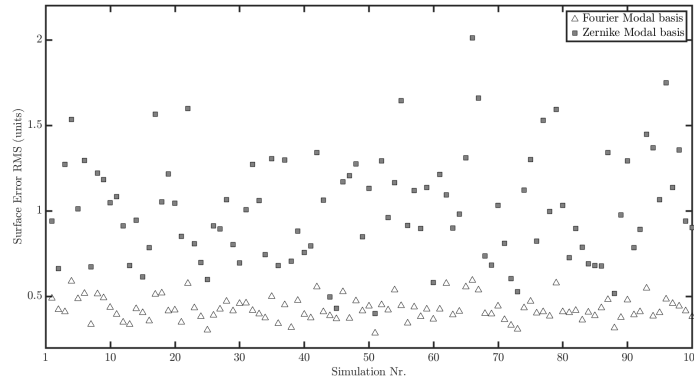


Figure A.3: Surface error of modal turbulence image reconstruction using a Zernike basis and a Fourier basis. The image shows that surface error is lower for the Fourier basis in all cases. The amount of modes used for both basis is 37 modes

A.3. DIFFERENTIATION OF THE FOURIER POLYNOMIAL TERMS FOR THE BI-HARMONIC EQUATION

This section provides a derivation of some Fourier modes into the plate bending equation in polar and cartesian coordinates to serve as proof of the possibility of satisfying the fourth order derivative. Fourier modes satisfying plate bending means they can be generated within a domain without necessity of satisfying outer boundary conditions. This in term means that, in theory, Fourier modes can be generated using actuation points within the aperture of the mirror thus maximizing focal aperture.

$$\Delta^2 \varphi = \frac{\partial^4 \varphi}{\partial x^4} + \frac{\partial^4 \varphi}{\partial x^2 \partial y^2} + \frac{\partial^4 \varphi}{\partial y^4} \quad (\text{A.7})$$

First mode (skip the angular frequency and assume the first mode to be at $f = 1/2\pi$)

$$\varphi = \sin(x) * \cos(y) \quad (\text{A.8})$$

where

$$\frac{\partial \varphi}{\partial x} = \cos(x)\cos(y) + 0; \quad \frac{\partial^2 \varphi}{\partial x^2} = -\sin(x)\cos(y) + 0; \quad \frac{\partial^3 \varphi}{\partial x^3} = -\cos(x)\cos(y) + 0; \quad (\text{A.9})$$

$$\frac{\partial^4 \varphi}{\partial x^4} = \sin(x)\cos(y) + 0 \quad (\text{A.10})$$

$$\frac{\partial}{\partial y} \left(\frac{\partial^2 \varphi}{\partial x^2} \right) = \sin(x)\sin(y) + 0; \quad (\text{A.11})$$

$$\frac{\partial^4 \varphi}{\partial x^2 \partial y^2} = \sin(x)\cos(y) + 0 \quad (\text{A.12})$$

Similarly:

$$\frac{\partial \varphi}{\partial y} = -\sin(y)\sin(x) + 0; \quad \frac{\partial^2 \varphi}{\partial y^2} = -\cos(y)\sin(x) + 0; \quad \frac{\partial^3 \varphi}{\partial y^3} = \sin(y)\sin(x) + 0 \quad (\text{A.13})$$

$$\frac{\partial^4 \varphi}{\partial y^4} = \sin(x)\cos(y) \quad (\text{A.14})$$

And:

$$\Delta^2 \varphi = 3\sin(x)\cos(y) \quad (\text{A.15})$$

Using Vdovins approach we can write the following:

$$\begin{aligned} 3\sin(x)\cos(y) &= \frac{q}{D} \rightarrow \int \int_C 3\sin(x)\cos(y)\partial x\partial y = \int \int_C \frac{q}{D} \partial p \\ &\rightarrow \int \int_C 3\sin(x)\cos(y)\partial x\partial y = \sum_{k=1}^N \frac{q}{D} \partial p \end{aligned} \quad (\text{A.16})$$

where q is a point load and D the flexural rigidity.

A.4. GENERAL DERIVATION FOR POLAR COORDINATES

The biharmonic equation in Polar coordinates reads:

$$\frac{1}{r} \frac{\partial}{\partial r} \left(r \frac{\partial}{\partial r} \left(\frac{1}{r} \frac{\partial}{\partial r} \left(r \frac{\partial \varphi}{\partial r} \right) \right) \right) + \frac{2}{r^2} \frac{\partial \varphi^4}{\partial \theta^2 \partial r^2} + \frac{1}{r^4} \frac{\partial^4 \varphi}{\partial \theta^4} - \frac{2}{r^3} \frac{\partial^3 \varphi}{\partial \theta^2 \partial r} + \frac{4}{r^4} \frac{\partial \varphi^2}{\partial \theta^2} = \frac{q}{D} \quad (\text{A.17})$$

If, $\varphi = \sin(nrcos\phi)\sin(nrcos\phi)$. Then the above expression reads:

$$\begin{aligned} \frac{1}{r} \frac{\partial}{\partial r} \left(r \frac{\partial}{\partial r} \left(\frac{1}{r} \frac{\partial}{\partial r} \left(r \frac{\partial \sin(nrcos(\phi)) \sin(nrcos(\phi))}{\partial r} \right) \right) \right) + \frac{2}{r^2} \frac{\partial^4 \sin(nrcos(\phi)) \sin(nrcos(\phi))}{\partial \theta^2 \partial r^2} + \\ \frac{1}{r^4} \frac{\partial^4 \sin(nrcos(\phi)) \sin(nrcos(\phi))}{\partial \theta^4} - \\ \frac{2}{r^3} \frac{\partial^3 \sin(nrcos(\phi)) \sin(nrcos(\phi))}{\partial \theta^2 \partial r} + \frac{4}{r^4} \frac{\partial \sin(nrcos(\phi)) \sin(nrcos(\phi))^2}{\partial \theta^2} = \frac{q}{D} \end{aligned} \quad (\text{A.18})$$

Where $n = 2\pi f$ and $x = r \cos(\phi)$, $y = r \sin(\phi)$. First, we derivate the r terms:

$$\frac{\partial \varphi}{\partial r} = n \cos \phi \cos(nrcos\phi) \sin(nrsin\phi) + n \sin \phi \sin(nrcos\phi) \cos(nrsin\phi) \quad (\text{A.19})$$

$$\begin{aligned} \frac{\partial}{\partial r} \left(r \frac{\partial \varphi}{\partial r} \right) = n \cos \phi \cos(nrcos\phi) \sin(nrsin\phi) - r n^2 \cos^2 \phi \sin(nrcos\phi) \sin(nrsin\phi) \\ + r n^2 \cos \phi \sin \phi \cos(nrcos\phi) \cos(nrsin\phi) + n \sin \phi \sin(nrcos\phi) \cos(nrsin\phi) \\ + r n^2 \sin \phi \cos \phi \cos(nrcos\phi) \cos(nrsin\phi) - n^2 \sin^2 \phi \sin(nrcos\phi) \sin(nrsin\phi) \end{aligned} \quad (\text{A.20})$$

$$\frac{\partial}{\partial r} \left(\frac{1}{r} \frac{\partial}{\partial r} \left(r \frac{\partial \varphi}{\partial r} \right) \right) = \quad (\text{A.21})$$

This term is needed for the cross derivatives:

$$\begin{aligned} \frac{\partial^2 \varphi}{\partial r^2} = -n^2 \cos^2 \phi \sin(nrcos\phi) \sin(nrsin\phi) + n^2 \sin \phi \cos \phi \cos(nrcos\phi) \cos(nrsin\phi) + \\ n^2 \sin \phi \cos \phi \cos(nrcos\phi) \cos(nrsin\phi) - n^2 \sin^2 \phi \sin(nrcos\phi) \sin(nrsin\phi) \end{aligned} \quad (\text{A.22})$$

B

LAYOUTS PERFORMANCE

B.1. POWER CONSUMPTION

This section compares the power consumption for a rectangular, hexagonal and circular arrangement of actuators. The IFs from the parametric simulations are modeled for a Force 1 N; this means that the term \bar{I}_n in 3.2 is a vector of ones and the least square fit values of \bar{I}_θ are the Forces needed to drive the mirror. By comparing the Standard Deviation (std) of all the individual forces required to drive the mirror to each of the aberration profiles described in 5.1, a plot like the one from Figure B.1 can be obtained.

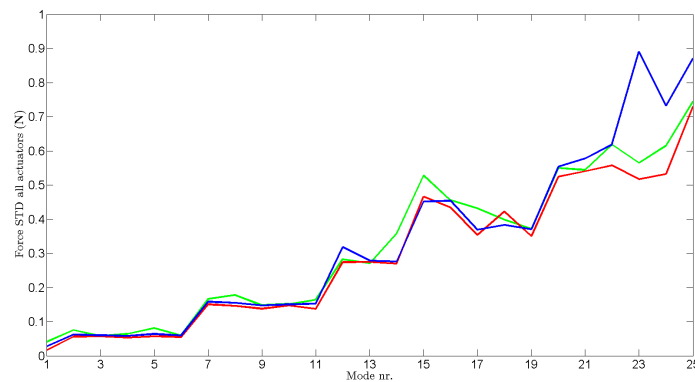


Figure B.1: $\sigma_f = \sqrt{f_1^2 + \dots + f_5^2}$ of all the Force values needed to generate each mode from the modal basis. The blue line is the square layout. The red line, the circular layout and the green curve belongs to the hexagonal arrangement

Figure B.1 shows there is small variation in power dissipation regardless of the used arrangement. However, the hexagonal arrangements shows an overall poorer performance. At higher order modes, circular layouts perform better.

B.2. ATMOSPHERIC TURBULENCE COMPENSATION FOR DIFFERENT LAYOUTS AND VALUES OF THE FILL FACTOR

Using the approach described in section 5 the approach from previous section is used and 20 simulations are run

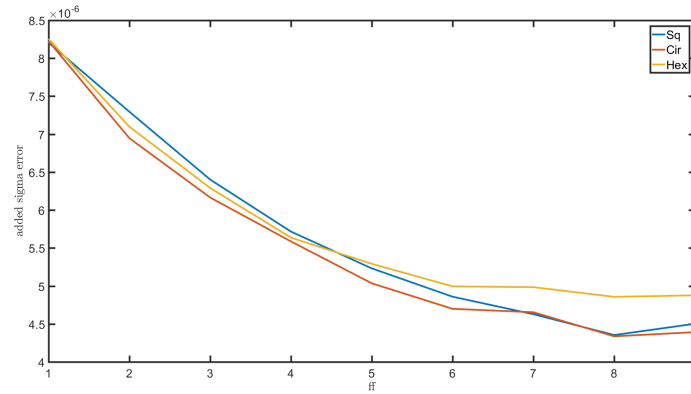


Figure B.2: Added rms of Monte Carlo style simulation for different ff and three layouts of the compensation of random Kolmogorov phase maps

B.3. DIFFERENT ACTUATOR COUNTS IN DIRECT RECONSTRUCTION OF KOLMOGOROV PHASE MAPS

In this analysis, different numbers of actuators arranged in a square layout are analyzed. The approach is the same as that of section 5.1. Kolmogorov phase screens are compensated using each actuator layout. Trends are clear; note how close the error is for the layouts with actuator counts 69, 57 and 45.

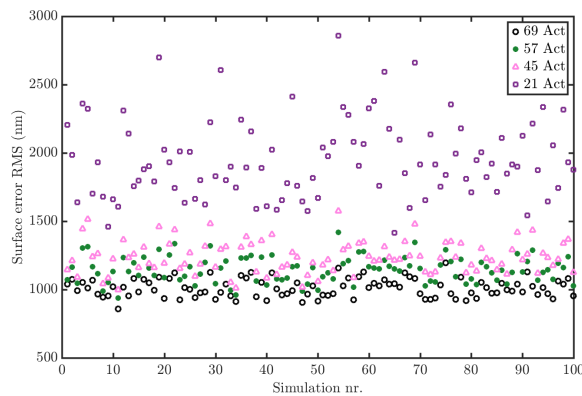


Figure B.3: Added rms of Monte Carlo style simulation for different actuator counts (69, 57, 45 and 21 actuators) in compensation of random Kolmogorov phase maps

C

ASSEMBLY OF THE 3D MODEL

Here, the assembly of the 3D model that emulates the flattening procedure is described. A least square fit approach is used to drive the modeled surface to a flatter shape. Three software were used to achieve this: MATLAB, for processing the best flat images, interpolate them and to run the LS algorithm. SOLIDWORKS, to generate a surface from the image data. And ANSYS WorkBench (Mechanical), for running simulations.

C.1. EXTRAPOLATION OF INTERFEROMETER IMAGE AND PREPARATION OF DATA

The interferometer images of the resting mirror surface can be uploaded to MATLAB using the code from section C.4. The code for the extrapolation of the initial flat to the full domain is described below and follows the theory from 4.2.

```
%% Extrapolation of initial flat to 160 mm diam. Make a regressor, extract
% regression variables, make regressor for bigger domain and multiply by
% regression vector
IFdomain = Flatness.data; % Original Interferometer image
% Create reduced domain
[X,Y] = meshgrid(Flatness.pos, Flatness.pos);
% Take out NaN's
xf = X(~isnan(IFdomain));
yf = Y(~isnan(IFdomain));
% Define frequencies for modal decomposition
fmax = 5;
freqs = (1:fmax)';
% Make columns for the regression matrix with sinusoidal waves
sinx = sin(freqs*xf'*pi)';
cosx = cos(freqs*xf'*pi)';
siny = sin(freqs*yf'*pi)';
cosy = cos(freqs*yf'*pi)';
% Make regression matrix (for small domain)
regr = [ones(length(sinx),1) sinx cosx siny cosy];
for i = 1:length(freqs)
    for j = 1:length(freqs)
        regr = [regr sinx(:,i).*siny(:,j) sinx(:,i).*cosy(:,j)...
                cosx(:,i).*siny(:,j) cosx(:,i).*cosy(:,j)];
    end
end
% Find regression variables
```

```

decomposition = regr\IFdomain(~isnan(IFdomain));
% Make regression matrix columns to create the big domain
sinX = sin(freqs*xd(:)'*pi)';
cosX = cos(freqs*xd(:)'*pi)';
sinY = sin(freqs*yd(:)'*pi)';
cosY = cos(freqs*yd(:)'*pi)';
% Store columns and make Matrix
Regr = [ones(size(xd,1)^2,1) sinX cosX sinY cosY];
for i = 1:length(freqs)
    for j = 1:length(freqs)
        Repr = [Regr sinX(:,i).*sinY(:,j) sinX(:,i).*cosY(:,j)...
                cosX(:,i).*sinY(:,j) cosX(:,i).*cosY(:,j)];
    end
end
% With regression variables and big regression matrix reconstruct domain
fulldom_nomask = Repr*decomposition;
fulldom_nomask = reshape(fulldom_nomask ,size(xd,1) , size(xd,1));

% Create .txt file for SW. CENTERED EXTRAPOLATION
% Make circular mask
mask_rC = (xd).^2+(yd).^2;
mask_rC(mask_rC>(0.08^2)) = NaN;
mask_rC(~isnan(mask_rC)) = 1e3;
fulldom_nonCenter = fulldom_nomask.*mask_rC;
% Make higher Extrapolation amplitude #'s smaller
fulldom_nonCenter(fulldom_nonCenter <-5e-3) = -5e-3;
fulldom_nonCenter(fulldom_nonCenter >5e-3) = 5e-3;

% Prepare data to be read as CloudPoint in solidWorks and save
[xmap , ymap] = meshgrid(0:160/length(fulldom_nonCenter):160- ...
    160/length(fulldom_nonCenter) , ...
    0:160/length(fulldom_nonCenter):160-160/length(fulldom_nonCenter) );
FlatDataFEM = [xmap(:) ymap(:) fulldom_nonCenter(:)];
FlatDataFEM( isnan(fulldom_nonCenter) ,:) = [];
save('C:\PointCloud' , FlatDataFEM , '.txt ')

```

C.2. SOLIDWORKS PROCESSING

The generated file (PointCloud) must be imported as a cloud of points in *SolidWorks*. Using mesh prep wizard, generate a mesh for the surface. All the options can be set to default except for the Orientation option which should be "none". Depending on the amount of points from the .txt file, it might be needed to down sample by reducing the detail of the mesh. Next, run the surface wizard and save the resulting surface as a *Parasolid* file.

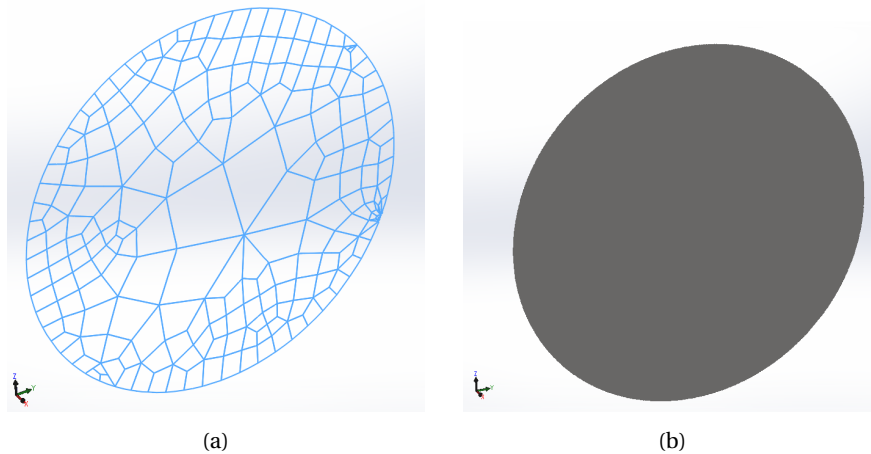


Figure C.1: (a) Mesh generated by *SolidWorks*. (b) Surface generated by *SolidWorks*

C.3. FEM ANALYSIS

For the FEM analysis, *ANSYS Workbench* was used. The simulation is a *Static Structural* analysis and the geometry must be uploaded externally. The *Parasolid* file from section C.2 is used. The material properties must be personalized to according to table ???. After that, the Coordinate origin is set to the center of the mirror. Then, the actuation points must be defined individually. This may be done by generating 57 individual named selections. To do this, in scope method the worksheet option is chosen and the OY coordinate is filtered for every OX coordinate of the actuators. All of the Boundary Conditions (rotation and displacement) will be established in the macro file which will run the simulation.

The first step to take in the simulations is to extract the Influence functions of the actuators. This is done using the following macro which must be included as a command snippet in the *Static Structural* section:

```

!!      APPLY STIFFNESS TO ACTUATOR NODES
ARG1 = 760
ARG2 = 760000
* if ,ARG1,LE,0 , then
  *MSG,ERROR
  ARG1 for Normal Stiffness on XYZ Elastic Foundation must be positive
  /EOF
  *return, -1
* endif
* if ,ARG2,LE,0 , then
  ARG2=ARG1
  /COM,##### ARG2 was made equal to ARG1 #####
* endif
fini
/prep7
*get,nodemax,NODE, ,NUM,MAX           ! highest node number in model
cmsel,s,Elastic_Here                 ! nodes of the component "Elastic_Here"
esln                                  ! select contacting elements
! unselect surface effect , contact , MPC and beam elements
esel,u,ename,,151,154
esel,u,ename,,169,180
esel,u,ename,,188,189
*get,maxtype,ETYP, ,NUM,MAX          ! highest element type
*get, maxmat,MAT, ,NUM,MAX           ! highest material type
*get, maxreal,RCON, ,NUM,MAX        ! highest real constant

```

```

! Set maxtype, maxmat and maxreal to the highest value of all three
* if , maxtype , gt , maxmat , then
    maxmat=maxtype
* else
    maxtype=maxmat
* endif
* if , maxreal , gt , maxtype , then
    maxtype=maxreal
    maxmat=maxreal
* else
    maxreal=maxtype
* endif
! Create required element types and real constant
ET,maxtype+1,CONTA174,,1,,0,3 ! Pure Penalty contact algorithm (stiffness)
KEYOPT,maxtype+1,9,1 ! Exclude geometrical gap
KEYOPT,maxtype+1,12,5 ! Bonded Always
ET,maxtype+2,TARGE170,,1 ! Constraints by user
R,maxreal+1,0,0,-ARG1,, -abs(ARG3) ! FKN Absolute Number
RMODIF,maxreal+1,12,-ARG2 ! FKT as Absolute Number
TYPE,maxtype+1 ! CONTA174 elements
REAL,maxreal+1
MAT,maxmat+1
ESURF ! Mesh CONTA174 over underlying element faces
*get , current_nodemin , node , , num , min
esln , r , 1 ! Select only these CONTA174 elements
esel , r , ename , , 174 ! Ensure no other elements
esel , r , real , , maxreal+1
! Make a copy of the currently selected nodes
NGEN,2,(nodemax-current_nodemin)+1,ALL,,0,0,0 ! Copy nodes atlocation
EGEN,2,(nodemax-current_nodemin)+1,ALL,,0,1,0 ! Copy elements TYPE by 1
esel , r , type , , maxtype+2 ! Select these new TARGE170 elements
ENSYM,0,,0,ALL ! Reverse TARGE170 elements to face contacts
nsle ! Select nodes on these target elements
d , all , all ! Constrain all nodes on target elements
allsel
! APPLY DISPLACEMENT LOADS HERE
*dim,qa,,18
qa(1) = ! Copy contents of .txt files generated by matlab and stored as iter1qa
*dim,qb,,18
qb(1) =
*dim,qc,,18
qc(1) =
*dim,qd,,3
qd(1) = -15.223,2.2675,-6.2927
*do , i , 1 , 57 , 1
*IF , i , lt , 19 , then
F , Selection_%i% , FZ , qa ( i )
*ELSEIF , i , lt , 37
F , Selection_%i% , FZ , qb ( i - 18 )
*ELSEIF , i , lt , 55
F , Selection_%i% , FZ , qc ( i - 36 )
*ELSE
F , Selection_%i% , FZ , qd ( i - 54 )
*ENDIF

```

```
*enddo
nsel, all
fini
/solu
```

Those IFs must then be imported to MATLAB using the procedure described in section C.4. Then, in a similar fashion to the procedure described in 3.2. The initial flat will also be processed using that method. To load the initial flat, the initial configuration of the mesh needs to be uploaded to MATLAB. The from C.4 is then used to determine the first set of Forces to be supplied to the mirror. The first simulation is ran by supplying the values found in the .txt files generated by MATLAB to lines 63, 65, 67 and 69 of the macro file above. The loop continues by repeating this process for several iterations.

C.4. PROCESSING IN MATLAB

With MATLAB, the control algorithm is ran in the same way as for the DM prototype. Firstly, the IFs are stored into a matrix. Then an initial flat file is loaded from the same set of measurements and turned into and turned into a matrix. After, the extrapolated part of the domain ($\varphi > 107$ mm) is masked (it is interpolated data and therefore is not useful) for both the IFs and the loaded Initial flat. Following the approach from 3.2 the SVD procedure is used and the resulting regression variables, which are multiplied by a normalized Force of 1 N are saved into .txt files for ease of copying into the macro. Each iteration a new displacement field is loaded, processed and added to the initial flat data to repeat the regression procedure.

```
% Load FEM 3D WB Analysis Flatness.
nr = 'file41'; % Choose ANSYS .xls output file
% Input here simulation processing code... Last line shown below:
zdom0 = F0(ydom,xdom);
load('K3da') % Load (shape functions) Kmatrix for the model
%% Reduce domain size to IF aperture
desmm = 51; % Radius desired mm
trgt = round(sqrt(size(K3da,1))*desmm/160);
[ci, cj] = meshgrid(-sqrt(size(K3da,1))/2:sqrt(size(K3da,1))/2-1,...
    -sqrt(size(K3da,1))/2:sqrt(size(K3da,1))/2-1 );
cr = (ci.^2+cj.^2);
cr(cr>trgt^2) = NaN;
cr = cr.*0+1;
% Reduce aperture
for i=1:size(K3da,2)
    K = reshape( K3da(:, i) , sqrt(size(K3da,1)) , [] );
    K = K.*cr;
    K_iterations(:, i) = K(:);
end
% Suppress nans for SVD
K_iterations(isnan(K_iterations)) = 0;
%% Flattening 1st iter
% Apply circular mask filter
zdom0 = zdom0.*cr;
% 0 instead of NaN
zdom0(isnan(zdom0)) = 0;
% SVD and normalization
disp_norder = K_iterations\zdom0(:);
norm = max(K_iterations(:,19));
disp = disp_norder;
% Store the actuation commands
```

```
deltas(1,:) = -disp';
% Write to txt with commas to be copied to clipboard
dlmwrite('1iterqa.txt', deltas(1,1:18))
dlmwrite('1iterqb.txt', deltas(1,19:36))
dlmwrite('1iterqc.txt', deltas(1,37:54))
dlmwrite('1iterqd.txt', deltas(1,55:end))
%% Load the 1st iteration and visualize it
nr = 'file42';
% Input here simulation processing code... Last line shown below:
zdom1 = F1(ydom,xdom);
% Interpolation displacement field
Flit = TriScatteredInterp( dxy , data1(:,4) );
dis1 = Flit(ydom,xdom);
% Add the domains to see the final shape
zdisp1 = zdom1+dis1;
reduced1 = zdisp1.*cr;
zdom1red = zdom1.*cr;
%% Second iteration
reduced1(isnan(reduced1)) = 0;
% SVD
disp_norder2 = K_iterations\reduced1(:);
disp2 = disp_norder2; % In ANSYS multiply again times 1e-3
%(to get rid of exponential numbering)
deltas(2,:) = -disp2';
dl2 = sum(deltas,1);
dlmwrite('2iterqa.txt', dl2(1,1:18))
dlmwrite('2iterqb.txt', dl2(1,19:36))
dlmwrite('2iterqc.txt', dl2(1,37:54))
dlmwrite('2iterqd.txt', dl2(1,55:end))
%% Load 2nd iteration Results... Repeat until reaching convergence
```

D

PARAMETRIC MODELING

The parametric approach uses ANSYS mechanical. Simulations are assembled as macro files which load automatize the simulation process. By using for loops, iterations can be made over design variables such as: Mirror thickness (shell element thickness), actuator stiffness and other. Below, an example of a macro which loops over stiffness values and extracts one influence function:

```
fini
/clear, nostart
*del, all
/prep7
ET,1,SHELL281           !Element types
ET,2,COMBIN14
R,1,1E6                 !Act stiffness
thickness_mirror = 1E-3 ! DEFINE MIRROR THICKNESS
MPTEMP,,,,,,,,
MPTEMP,1,0
MPDATA,EX,1,,70E9      ! Elastic modulus
MPDATA,PRXY,1,,0.33    ! Major Poission's ratio
sect,1,shell,,
secdata, thickness_mirror,1,0.0,3
secoffset,MID
seccontrol,,,,,
QRad = 80E-3           ! DEFINE RADIUS OF MIRROR
QradF = Qrad*0.90      !Placing area
badrad = sqrt(2*((18E-3)*3)**2)
cyl4,0,0,QRAD
NUML = 9               ! Actuator locations are set
*DO,i,1,NUML
    k,4+(2*i)-1,-QRad,-QRadF + QRADF/((NUML-1)/2)*(i-1),0
    k,4+(2*i),QRad,-QRadF + QRADF/((NUML-1)/2)*(i-1),0
    l,4+(2*i)-1,4+(2*i)
*enddo
ASBL,1,ALL
*get,maxK,kp,,num,maxd
*DO,i,1,NUML
    k,maxK+(2*i)-1,-QRadF + QRADF/((NUML-1)/2)*(i-1),-QRad,0
    k,maxK+(2*i),-QRadF + QRADF/((NUML-1)/2)*(i-1),QRad,0
    l,maxK+(2*i)-1,maxK+(2*i)
```

```

*enddo
ASBL,ALL,ALL
!*GET, Par, Entity, ENINUM, Item1, IT1NUM, Item2, IT2NUM
*get,qnumk,kp,,count
*dim,qkeyploc,array,qnumk
*dim,qkxi,array,qnumk
*dim,qkyi,array,qnumk
ksel,all
*vget,qkeyps,kp,,klist
index = 0
*do,i,1,qnumk
  *get,qkx,kp,qkeyps(i),loc,x
  *get,qky,kp,qkeyps(i),loc,y
  locr = sqrt(qkx**2 + qky**2)
  *if,locr,lt,Qrad,AND,locr,NE,badrad,then
    index = index + 1
    qkeyploc(index)=qkeyps(i)
    qkxi(index) = qkx
    qkyi(index) = qky
  *endif
*enddo
AESIZE,all,1E-3,      ! Mesh
amesh,all
type,2                ! Add stiffness supports
*do,i,1,index
  nsel,none,
  nsel,s,loc,x,0.999*qkxi(i),1.0001*qkxi(i)
  nsel,r,loc,y,0.999*qkyi(i),1.0001*qkyi(i)
  *get,qn%i%,node,0,num,max
  n,100000+i,qkxi(i),qkyi(i),-1E-2
  n,200000+i,qkxi(i)-1E-2,qkyi(i),0
  n,300000+i,qkxi(i),qkyi(i)-1E-2,0
  nsel,all
  e,qn%i%,100000+i
  d,100000+i,all,0
  e,qn%i%,200000+i
  d,200000+i,all,0
  e,qn%i%,300000+i
  d,300000+i,all,0
*enddo
! Place loop for varying stiffness
/eof
*do,st,1,15
RMODIF,1,1,(6.2+0.2*st)*1E4
nact = 21
DK,qkeyploc(nact),UZ,1.8E-6      ! Prescribe displacement
/solu  ! Solver
solve
FINISH
/post1
plnsol,u,z
nsel,s,loc,z,0
*vget,nodes_top,node,1,nlist
nsel,s,loc,z,0

```

```

NSEL, s, node, , 1,100000-1
*get,num_of_nodes_at_top,node,,count
*dim,disp_z,array,num_of_nodes_at_top
*dim,nodes_x,array,num_of_nodes_at_top
*dim,nodes_y,array,num_of_nodes_at_top
j=1
*do,i,1,num_of_nodes_at_top
*get,temp_x,node,nodes_top(i),loc,x
*get,temp_y,node,nodes_top(i),loc,y
*get,temp_uz,node,nodes_top(i),u,z
disp_z(j)=temp_uz
nodes_x(j) = temp_x
nodes_y(j) = temp_y
j = j+1
*enddo
*cfopen,iterstifref%st%,txt
*vwrite,nodes_top(1),nodes_x(1),nodes_y(1),disp_z(1)
(F8.0,3E20.10)
*cfclose
/prep7
*del,disp_z
*del,nodes_x
*del,nodes_y
DKDELE,qkeyploc(nact),ALL      ! Delete force on actuator
*enddo
!/solu
!*SMAT,Stiff_Matrix,D,IMPORT,FULL,file.full,Stiff
!*EXPORT,Stiff_Matrix,MME,Stiff_Matrix.dat

```

The simulation results are stored as .txt files which are processed in MATLAB:

```

sim_direct = 'C:\FEM_DM\APDL\10022017\';% Simulation directory?
simulation_name = 'actID';           % How are files saved?
number_of_files = 10; % How many files in simulation folder?
for nr=1:number_of_files
    fload = strcat(simulation_name , num2str(nr));
    raw_data = dlmread(strcat(sim_direct , fload , '.txt'));
    raw_data(:,1) = [];
    data = sortrows(raw_data,1);      % Sort x ascending
    % Interpolate domain values
    dxy = [data(:,1) data(:,2) ];
    dz = data(:,3) ;
    F = TriScatteredInterp( dxy , dz );
    % Take out repeated instances
    xg = unique(data(:,1));
    yg = unique(data(:,2));
    % Create domain for plotting
    [xdom , ydom] = meshgrid(xg(1):30/length(xg):xg(length(xg)),...
        yg(1):30/length(yg):yg(length(yg)));
    M_shf = F(ydom,xdom);
    % Store influence function
    modeled(nr).data = M_shf;
end

```

D.1. MATLAB-ANSYS COUPLING

ANSYS and MATLAB can be coupled when running the FEM software in the background using a .bat file. MATLAB will start ANSYS, wait for it to run simulations and then process the information from the simulations. More on this philosophy can be found in [29]. To run ANSYS from batch, a .bat file containing the following lines is needed:

```
SET KMP_STACKSIZE=2048k & "C:\Program Files\ANSYS Inc\v171\ansys\bin\winx64\ANSYS171.exe"
-dir "C:\AlejandroLocal\Projects\DeformableMirror\DesignOptim\Matlab\work"
-b -i opthc.mac -o out.txt -j optimize & exit
```

The MATLAB code used is shown below:

```
% Assert there is not an existing stand-by file
if exist('ansys_wait.txt','file')
    delete('ansys_wait.txt')
end
% Check for lock files (They block ANSYS)
if exist('ansysfiles.lock','file')
    delete('ansysfiles.lock')
    error('It is required to delete .lock file in working directory manually')
end
% Declare objective function [Size is known from trial with ANSYS]
obj_sz = 120;
ob = Fourier_basis(0,3,obj_sz,'dele');
for i=1:length(ob)
    ob(i).data(isnan(ob(i).data))= 0;
    ob(i).data = ob(i).data*1e-6;
end
% Assign values to Thickness of the facesheet and Pitch to iterate
ss1 = [50e-6 0.1e-3];
ss2 = [100e3 1000e3];
% Define pitch for simulation
pitch = 18e-3;
f = fopen('pitch.txt','wt');
fprintf(f,'%30.24e',pitch);
fclose(f);
% Maximum evaluations for the optimization procedure
maxiter = length(ss1)*length(ss2);
%Pre-allocate some variables
error = struct;
ni = 1;
nj = 1;
% Optimization Procedure
for i=1:maxiter
    %Extract parameters
    s(1) = ss1(ni);
    s(2) = ss2(nj);
    if nj == length(ss2)
        nj = 0;
        ni = ni+1;
    end
    nj = nj+1;
    % Send parameters to ANSYS
    f = fopen('parameters.txt','wt');
    fprintf(f,'%30.24e',s);
```



```
fclose(f);
% Start ANSYS
system('Couple_ANSYS.bat &');
% Wait while ANSYS is doing calculating
while exist('ansys_wait.txt','file')==0
end
% Load data from ANSYS and interpolate
act = 57; % #Acts to be loaded
mats = .5; % Declare size of matrix. NOTE: If changed, modify obj_sz
% Load influ func by influ func...
for nr=1:act
    % Input code for processing simulation data...
end
% If Matlab has the new parameters ready, it deletes the .txt file to
% start an iteration. In Matlab:
delete('ansys_wait.txt')
end
```

E

CONSTANT WIDTH OF THE INFLUENCE FUNCTION

This annex describes the methodology used for determining the width of the influence function. It was determined using the code listed below. From the input and output of the code (IFs with determined mechanical parameters and width respectively), curves can be constructed as has already been done several times through out the document.

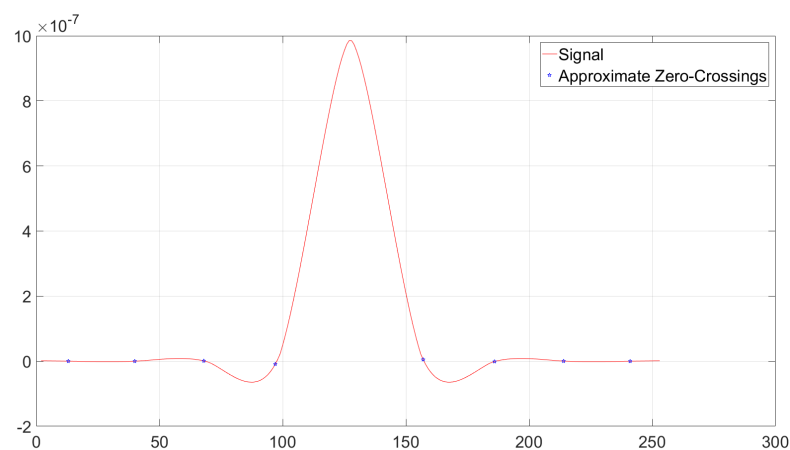


Figure E.1: Example of the matlab routine that captures the zero-crossings of the IF

```
% Load varying stiffness data
for nr=1:10
    fload = strcat('sw' , num2str(nr));
    raw_data = dlmread(strcat( 'O:\TNO\FEM_DM\APDL\09192017\' , ...
        fload , '.txt '));
    raw_data(:,1) = [];
    data = sortrows(raw_data,1);          % Sort x ascending
    dxy = [data(:,1) data(:,2) ];
    dz = data(:,3) ;
    F = TriScatteredInterp( dxy , dz );
    xg = unique(data(:,1));
```

```

    yg = unique(data(:,2));
    [xdom , ydom] = meshgrid(xg(1):sz/length(xg):xg(length(xg)), ...
        yg(1):sz/length(xg):yg(length(yg)));
    M_shf = F(ydom,xdom);
    modeled(nr).data = M_shf;
end

for nr=1:10
    a = modeled(nr).data(round(length(M_shf)/2),:);
    t = 1:length(a);
    zci = @(v) find(v(:).* circshift(v(:), ...
        [-1 0]) <= 0);% Returns Zero-Crossing Indices Of Argument Vector
    zx = zci(a);      % Approximate Zero-Crossing Indices
    figure(nr)
    plot(t, a, '-r')
    hold on
    plot(t(zx), a(zx), 'bp')
    hold off
    grid
    legend('Signal', 'Approximate Zero-Crossings')

    xin = zx.*160/length(a);

    if size(xin,1)>2
        dis = abs(xin-80);
        dis = sort(dis);
        dis(3:end) = [];
    elseif size(xin,1)==2
        dis = abs(xin-80);
    else
        dis = 0;
    end
    width(nr) = sum(dis)/2;
end

```

An interesting application of this approach is to determine constant ratios for IFs. This was done by using the points at which the sinc shape first appears. It was seen that the relations between tuning parameters i.e. the points at which a sinc shape appears when varying one or two parameters, follow a linear trend. Some examples of this and the varied parameters are shown below. The images show at which parameters of t , k and actuator pitch the sinc function appears. The ratio of single parameter variations is the same as the ratio of varying two parameters. It is therefore easy to predict where a certain IF will have the same shape when varying one, two or the three design parameters that were tested.

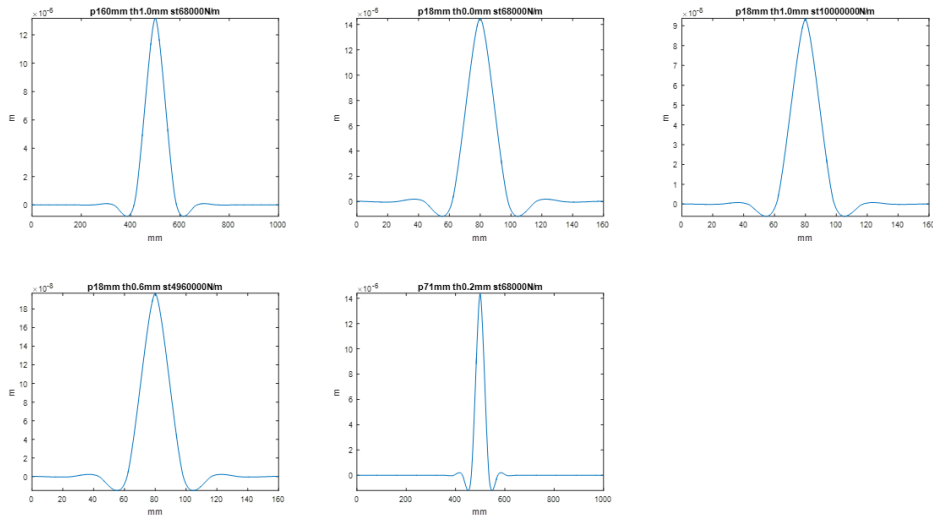


Figure E.2: Constant IF with a sinc function shape for different t , pitch and k values

	PITCH	STIFFNESS	THICKNESS
PITCH	P	PS	PT
STIFNESS		S	ST
THICKNESS			T

Figure E.3: Constant IF with a sinc function shape for different t , pitch and k values

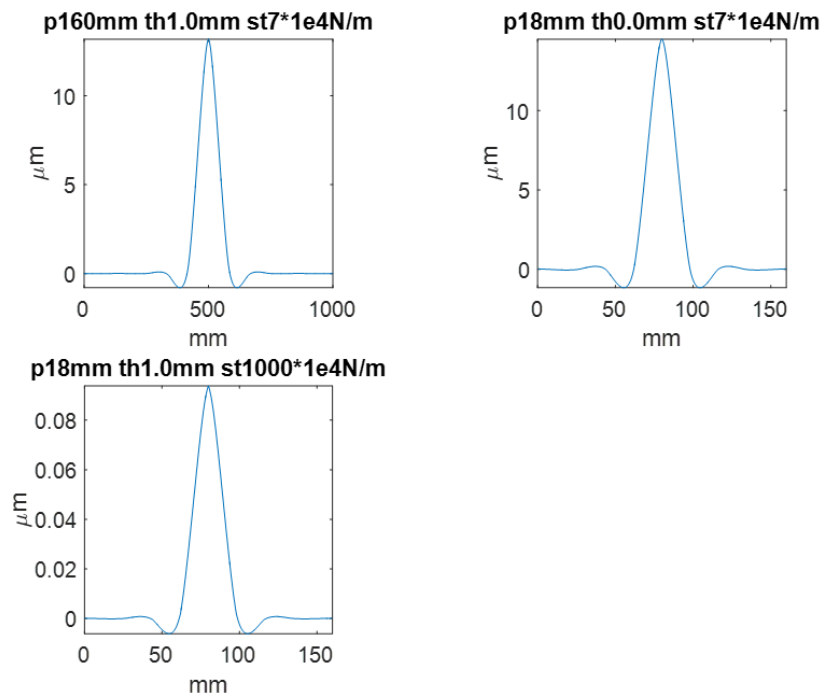


Figure E.4: Variation of a single parameter for constant IF case

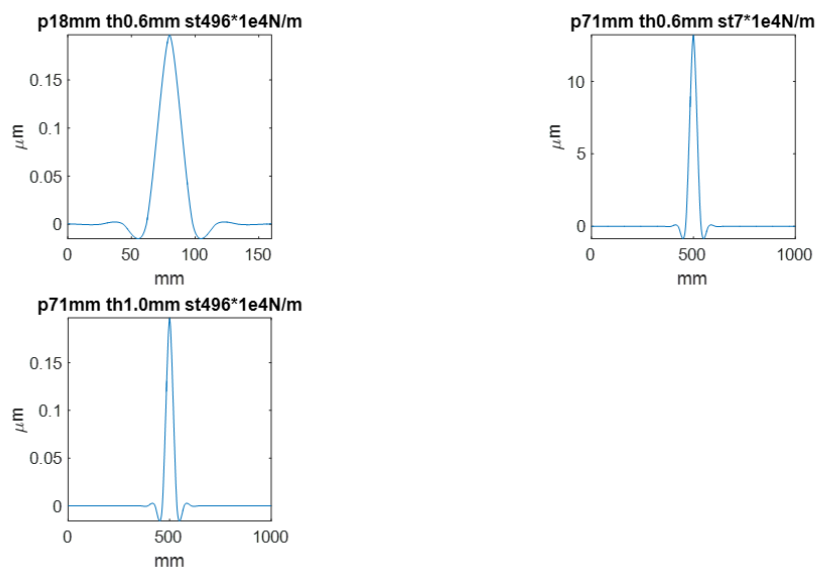


Figure E.5: Constant IF for two parameter variation